

A Comparative Analysis of CO Isotopologue Multi-Line Modeling of the Physical Conditions in the Starburst Galaxy M82

Valencia Zhang
Phillips Academy
180 Main Street
Andover, MA 01810, USA

Mentor: Dr. Jakob den Brok
Center for Astrophysics | Harvard & Smithsonian
60 Garden St.
Cambridge, MA 02138, USA

A Comparative Analysis of CO Isotopologue Multi-Line Modeling of the Physical Conditions in the Starburst Galaxy M82

VALENCIA ZHANG

ABSTRACT

The study of the physical conditions of cold molecular gas in the interstellar medium (ISM) is crucial to understanding star formation and galaxy evolution. Starburst galaxies are environments of extreme star-forming conditions with rich molecular gas content. Ratios of spectral line intensities of various CO isotopologues are a direct way to probe the conditions of molecular gas. A common approach to deriving the properties of molecular gas, such as temperature, volume density, and column density, is to compare these observed line ratios to ratios calculated by models of multi-line radiative transfer simulations. However, such models often assume a singular or dual gas phase, which oversimplifies the diverse nature and structure of the molecular ISM. In this paper, we analyze low- J rotational transitions of ^{12}CO , ^{13}CO , C^{18}O from sub(mm) observatories across the starburst M82. We develop and implement three different radiative transfer models of varying sophistication: a one zone model, a log-normal density distribution model, and a novel log-normal temperature distribution model. Using Bayesian maximum likelihood analysis, we derive the physical properties of starburst galaxy M82 by comparing observations to simulation models and contrasting the inferred values from each model. We show that line intensity ratios vary drastically across the central molecular zone of M82, indicating that physical conditions of the galaxy are also varying. We find that our one-zone model yields significantly different temperatures and densities from our log-normal models. This reveals that the specific prescription of multi-line modeling is critical. Overall, our results unravel the complex nature of starburst galaxies, from their molecular gas composition and conditions to their history during the peak of cosmic star formation.

Keywords: galaxies, star formation, molecular clouds, interstellar medium, multi-line modeling

1. INTRODUCTION

The interstellar medium (ISM) is the gas, dust, and particles that fill the space between stars in galaxies. In the ISM, gas and dust accumulate into cold and turbulent molecular clouds. These clouds are of extreme importance because stars form from the gas inside. Thus, to understand star formation and galaxy evolution, it is crucial to study the physical conditions that regulate the gas in molecular clouds.

Molecular clouds are primarily comprised of molecular hydrogen (H_2). However, emission from H_2 is not practically observable in cold gas (Togi & Smith 2016). This is because molecules have three types of excitation: electronic (when an electron is excited), vibrational (when the vibrational state of nuclei is excited), and rotational (when the rotational motion of the nuclei about the center of mass is excited). The extreme temperatures in the ISM are too cold to excite electronic and vibrational transitions of H_2 , which leaves rotational excitation as the only option (den Brok 2022). When a molecule rotates, it can only do so at a quantized energy level described by the rotational quantum number J . In the case of homonuclear H_2 , the lowest rotational energy transition is the $J = 2 \rightarrow 0$ transition (meaning a transition from rotational energy level 2 to 0), which has an upper energy level of $E/k_B \sim 510\text{K}$ (Dabrowski 1984; van Dishoeck & Black 1986; den Brok 2022). A dense cloud has a low temperature of less than 100K, and thus is also too cold to excite the rotational transitions of H_2 .

Then, in order to study the molecular gas in the ISM, we turn to proxies, which include dust emission and emission of other molecules. Of these proxies, observation of molecular line emission offers very sensitive and high resolution (sub-kpc scale) measurements in nearby galaxies with current millimeter observatories such as the Submillimeter Array (Krumholz & McKee 2005). The most common molecular gas tracer is carbon monoxide ($^{12}\text{C}^{16}\text{O}$, hereafter abbreviated as CO), which is made in the ISM when the C and O atoms combine (den Brok 2022). CO is the ISM's

second most abundant molecule and is an effective molecular tracer for H_2 because it has low excitation energy of only $E/k_B \sim 5\text{K}$. CO has multiple rotational energy transitions that can be excited even at the low temperatures of cold clouds. Hence, to probe molecular gas, it is crucial to observe low J energy transitions of CO.

While CO is an effective tracer of H_2 , there are still challenges in relying on the emission of CO because of optical depth (den Brok 2022). Optical depth describes how much a material blocks or absorbs light. When a medium is optically thick (opaque), it means that the medium is effectively absorbing and scattering light and does not give much information of what happens inside. As light passes through the medium, its intensity is significantly reduced. In the context of CO, emission from the CO $J = 1-0$ line is optically thick and therefore a significant fraction of emission from dense star-forming clouds is self absorbed (Shetty et al. 2011). This leads to a degeneracy in the intensity of this low J line (Teng et al. 2022). Specifically, this degeneracy exists because the intensity of the line depends on both the optical depth and column density of H_2 . When intensity increases, this could be a result of either a decrease in optical depth or an increase in mass of H_2 .

Therefore, to best constrain and determine the physical conditions and state of the molecular gas in the ISM, it is crucial to study optically thin tracers and specifically, their intensity ratios as well. Examples of optically thin tracers include less abundant CO molecular species with different isotopic compositions known as isotopologues. $^{13}\text{C}^{16}\text{O}$ (hereafter abbreviated as ^{13}CO) has a relatively low abundance ($\text{CO}/^{13}\text{CO} \sim 20 - 70$) and is generally optically thin (Langer & Penzias 1990; Tan et al. 2011; Shimajiri et al. 2014). Another CO isotopologue C^{18}O is another order of magnitude less abundant than ^{13}CO and, hence, is also optically thin (Wouterloot et al. 2008; Areal et al. 2018). To effectively trace changes in physical conditions of a galaxy, we must look to ratios of the isotopologue energy transitions. Variations in line ratio is linked to changes in the relative abundances of the isotopologues or variation in the physical properties of the gas, such as its opacity, temperature, or density (Davis 2014). Thus, CO isotopologues and their line ratios are crucial in disentangling the values and variances of physical parameters of molecular gas.

Several studies use low- J isotope transitions in conjunction with non local thermal equilibrium radiative transfer models to probe physical conditions in galaxies (see Eckart et al. 1990; Michiyama et al. 2018; Israel 2009, 2020). In these studies, it is assumed that the emission is either originating from a slab of gas with uniform physical properties (known as one component modeling or one zone modeling) or dominated by two distinct model gas phases (known as two component modeling). However, such models potentially over-simplify physical reality and do not accurately describe the diverse nature and environment of molecular clouds. For example, these models ignore that a molecular cloud can have varying temperature and density. Thus, to accurately prescribe the physical conditions and processes in the ISM, it is necessary to develop more sophisticated models and to see how these models affect inferred physical parameters (Israel 2020). Examples of such models include a log-normal density distribution, which follows from simulations (Vazquez-Semadeni et al. 1994; Elmegreen & Scalo 2004). A log-normal density distribution is a more sophisticated and realistic way to describe the cold molecular gas (Padoan & Nordlund 2002)¹. However, log-normal density distributions do not take into account changes in temperature. Further sophisticated models that include changing temperature among other parameters over a range of phases are therefore still needed.

In this paper, we investigate the physical properties of the star forming molecular gas in the Messier 82 (M82) galaxy. We contrast and analyze the results of three multi-line modeling approaches: a one zone model, a log-normal density distribution model (first application of such a model to M82), and a novel log-normal temperature distribution model (first ever implementation). The three models are non local thermal equilibrium models, so they do not assume the gas is in equilibrium. The latter two models employ a sophisticated probability density function, which assumes a smoothly changing density or temperature over a range of phases rather than a fixed value (see Leroy et al. 2017). We then assume local thermal equilibrium (LTE) to see how calculated results contrast with non-LTE models. We address the following questions: what are the varying physical conditions of M82’s molecular gas, and how does emission from CO isotopologues trace the underlying changes in the molecular gas conditions of M82? To what degree do the inferred molecular gas conditions depend on the particular multi-line model prescription?

This paper is organized as follows. In Section 2, we first introduce our target, outline the formation of CO data cubes, and show plots mapping our target. We then explain the method, implementation of our multi-line radiative transfer modeling, and our use of Bayesian maximum likelihood analysis. In Section 3, we first investigate CO line ratios to see how they qualitatively agree with variation in molecular gas conditions throughout the target. Finally,

¹ A log-normal distribution is a continuous probability distribution of a variable whose logarithm is normally distributed. The functional form can be found in 2.3.1.

to understand the physical state of the molecular gas, we compare observations to calculated values that assume local thermal equilibrium. In Section 4, we discuss our results and their implications. Finally, in Section 5, we conclude and discuss the broader impact of our paper.

2. OBSERVATIONS AND METHODS

2.1. Target

In this paper, we study the CO isotopologue emission of the galaxy Messier 82 (M82). M82 is a prime target for molecular gas studies because it is nearby ($D = 3.5$ Mpc) and has a high surface brightness, making fainter emission detectable (Lianou et al. 2019). M82 is also a starburst galaxy, which means it has extremely high star formation rate (SFR). M82 has a stellar mass of $5 \times 10^9 M_{\odot}$ and a SFR of 13 solar masses per year in comparison to the Milky Way Galaxy’s 1.7 solar mass per year (Sofue 1998; Förster Schreiber et al. 2003; Elia et al. 2022). In Figure 1, we plot the SFR versus the stellar mass of nearby ($z < 0.1$) galaxies from the Sloan Digital Sky Survey (SDSS) and a Hubble image of M82 in the upper left (Blanton et al. 2017; Kollmeier et al. 2019). In orange, we plot the band of main sequence galaxies, and we mark the Milky Way galaxy and M82 in a cyan dot and red star respectively. The blue histogram plots nearby galaxy populations. We see that M82 lies significantly above both the main sequence band and Milky Way, demonstrating its extreme nature. In the Hubble image of M82, we see dramatic plumes of hydrogen blasting out from central regions where stars are being born. Overall, M82 is a prime candidate to study molecular gas conditions using faint CO isotopologue line emission and investigate connections to star formation.

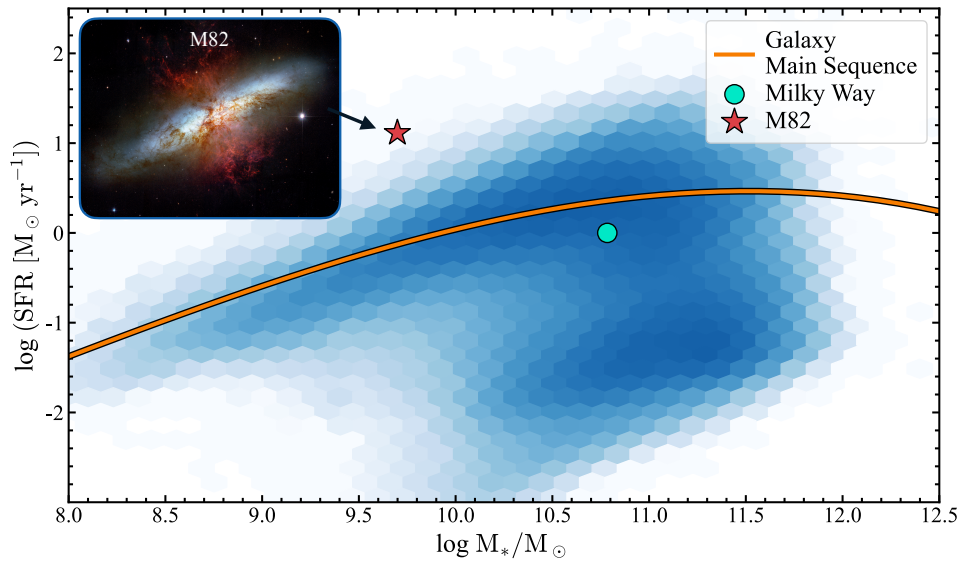


Figure 1. M82 and Milky Way annotated on plot of SFR vs stellar mass of nearby galaxy populations, Hubble image of M82 in top left corner. We highlight the main sequence galaxies with an orange band. The blue shaded histogram shows the distribution of nearby galaxy populations from SDSS (Blanton et al. 2017; Kollmeier et al. 2019).

Credit: NASA, ESA and the Hubble Heritage Team (STScI/AURA). Acknowledgment: J. Gallagher (University of Wisconsin), M. Mountain (STScI) and P. Puxley (NSF).

2.2. Data

As mentioned in 1, CO and its isotopes have energy transitions that can be excited in cold molecular clouds. These transitions all emit energy at sub(mm) wavelengths and can be observed with radio and far infrared telescopes.

2.2.1. Low Resolution Data and Calibration

We obtain low resolution data of 6 CO isotopologue energy transitions from the following three telescopes: the Nobeyama 45-m Radio Telescope (NRO45M), the IRAM 30m Millimeter Radio Telescope (IRAM30M), and the James Clerk Maxwell Telescope (JCMT). With a beam size of $\sim 20''$, we can constrain dynamics of the galaxy on a kpc-scale and see global trends across the galaxy (a resolution of $20''$ resolves a distance of 0.34 kpc). Our low resolution data

can resolve sub-kpc distance and allows us to trace all the larger-scale, kpc-scale variation across the galaxy. Table 1 summarizes the low resolution lines.

Table 1. Summary of Low Resolution CO lines.

Telescope	Line	Rest Frequency (GHz)	Beam Size (")	Physical Distance (kpc)
NRO45M	$^{13}\text{CO } J = 1-0$	110.201	17	0.29
NRO45M	$\text{CO } J = 1-0$	115.271	17	0.29
IRAM30M	$\text{C}^{18}\text{O } J = 2-1$	219.560	13	0.22
IRAM30M	$^{13}\text{CO } J = 2-1$	220.399	13	0.22
IRAM30M	$\text{CO } J = 2-1$	230.538	20	0.34
JCMT	$\text{CO } J = 3-2$	345.796	17	0.29

We use an upper and lower masking technique to isolate the signal. We first perform a conservative masking down to a high signal to noise ratio (S/N) of 4. Then, we perform a broader cleaning to collect all remaining emission down to a low $S/N = 2$. In the second step, we only add onto the original mask when there are at least three consecutive channels. An example of a masked spectrum can be seen in Figure 2. The masked spectrum in red picks up to the yellow root mean square line and neglects any pixels of low S/N ratio. There are two regions of emission which the mask captures. We then convolve the data to the finest possible beam size (beam size = 20" set by the $\text{CO } J = 2-1$ line). Finally, we use the $^{13}\text{CO } J = 1-0$ as the overlay file (the different data files do not share the same field of view so the overlay defines the region).

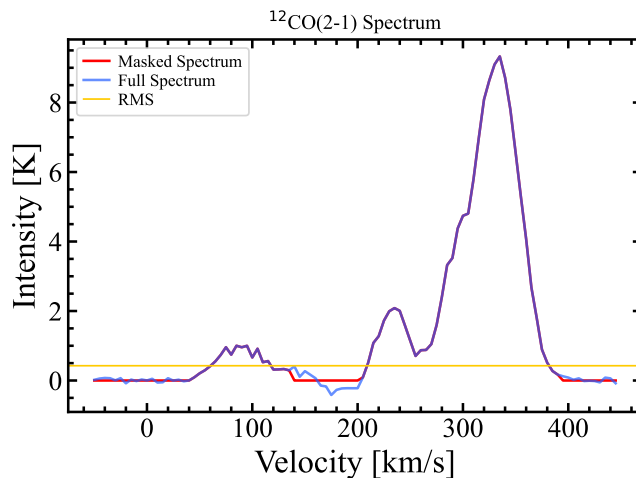


Figure 2. $^{12}\text{CO}(2-1)$ emission spectrum (blue), masked spectrum (red), RMS value (yellow). We plot intensity vs velocity. The spectra overlap in purple.

2.2.2. High Resolution Data and Calibration

We obtain high resolution data of 4 CO isotopologue energy transitions from the Submillimeter Array (SMA). With a much smaller beam size, we can constrain the dynamics of the gas on giant molecular cloud scales. Table 2 summarizes the high resolution lines.

As with low resolution processing, we use an upper and lower masking technique to isolate the signal from the noise. Our high mask threshold is a S/N of 6 and the low mask threshold is $S/N \sim 2$. Following the masking, we can calculate moments using this mask so that we do not account for contribution from noise. We then convolve the data to the finest possible beam size (beam size = 3.7" set by the $\text{C}^{18}\text{O } J = 2-1$ line. With an angular resolution of 3.7", we can resolve a spatial distance of ~ 60 pc) so that the final calibrated data cubes span the same spatial scale. Finally, we use the $\text{CO } J = 3-2$ as the overlay file. These calibration and imaging processes give high quality data cubes for the high resolution data.

Table 2. Summary of High Resolution CO lines.

Telescope	Line	Rest Frequency (GHz)	Beam Size (")	Physical Distance (pc)
SMA	C ¹⁸ O $J=2-1$	219.560	3.88	65.8
SMA	¹³ CO $J=2-1$	220.399	3.60	61.1
SMA	CO $J=2-1$	230.538	2.78	47.2
SMA	CO $J=3-2$	345.796	0.8	13.6

2.2.3. Final Data Cubes

Our final data cubes include calculation of the moment 0, moment 1, and moment 2. Moments provide a quantitative way to summarize and display data pertaining to molecular gas. Moment 0, also known as the velocity-integrated brightness temperature, is calculated by integrating intensity along the frequency axis with a channel width of δv (the frequency axis was converted to velocity). We only integrate for values included in the mask. For example, in Figure 2, we would only integrate from around a velocity of 200 km/s to 400 km/s. Moment 0 represents the intensity value or brightness of emission. Moment 1 represents the mean velocity of the molecular gas (hence, why we use a red blue colormap) and is calculated by summing over the moment 0 weighted by main beam temperature (again, only summing over the pixels in the mask). Finally, moment 2 estimates the velocity dispersion or the width of the emission line. Equations for moment calculations can be found in A.

Figure 3 shows the moment 0, 1, and 2 of the low resolution ¹²CO(2-1) transition. The x and y axis for all three figures is the difference in right ascension and declination as measured in arcseconds from the center of the galaxy determined by Jackson et al. (2007). The white contours on the moments trace out levels of intensity. The hexagonal grid is half beam sized, meaning that the pixels are separated by half the beam size. All other plots follow these spacing and axis conventions unless mentioned otherwise. Moments for all other transitions can be found in the Appendix.

We see from the middle panel of Figure 3 that there is a shift in blue-red along the minor axis of the galaxy, which indicates that the galaxy is rotating. We also see from the right panel that there are higher velocity dispersions toward the center.

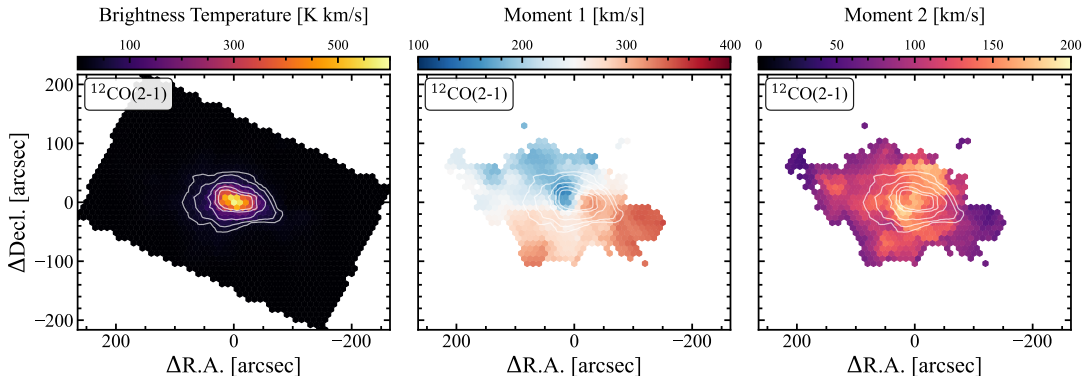


Figure 3. Moment 0, 1, 2 for Low Resolution ¹²CO(2-1) Transition. The left panel is moment 0, middle is moment 1, and right is moment 2.

Figures 4, 5, and 6 show the moment 0 (titled as Brightness Temperature), moment 1, and moment 2 calculated from the high resolution data cubes. We display all four line transitions in the following order: ¹²CO(2-1), ¹²CO(3-2), ¹³CO(2-1), and C¹⁸O. The x and y axis follow the same conventions as Figure 3. On Figure 4, we define the cardinal directions of north and east. On all moment maps, we also display white contours which trace out intensity levels.

We note that the spacial scale of high resolution and low resolution is significantly different. Low resolution data images a larger area and displays general trends of the galaxy but resolves less internal structures. In the high resolution Figure 4 specifically, we see much more shape in the galaxy with three knots of dramatically high intensity. Later in our analysis, we use these three knots as regions to compare line ratios (see 3.2).

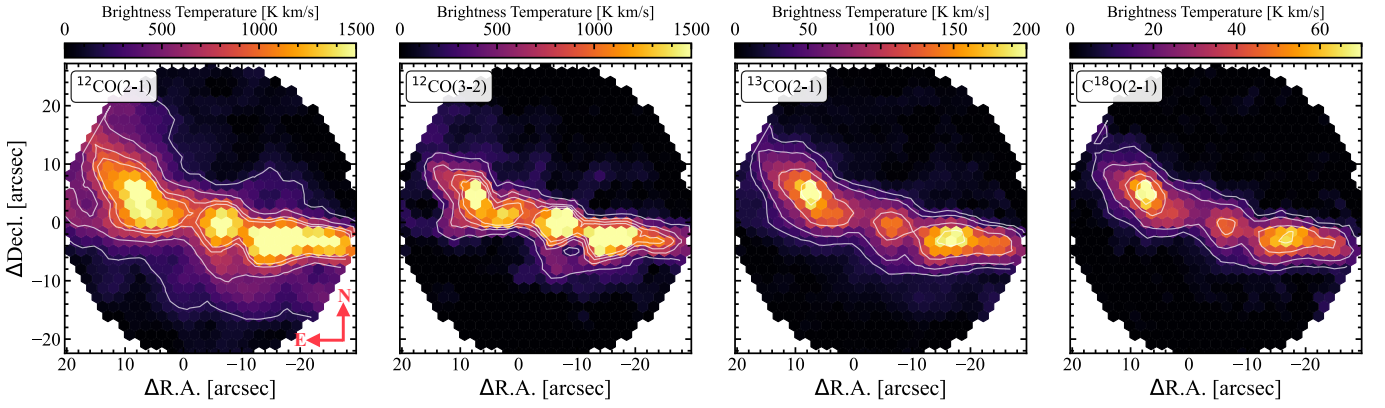


Figure 4. Moment 0 For High Resolution Data. We see three brighter knots along the disk of M82 and contours tracing out each region. Cardinal directions of moment maps is illustrated in the left panel.

The second and fourth panel of Figure 5 seems to follow a shape similar to that seen in Figure 4. From Figure 5, we see that the center of the galaxy is moving away from our line of sight at around 200 km/s. Eastern regions of the galaxy are moving away from the line of sight faster and western regions move away slower. This indicates that the galaxy is rotating. The axis by right hand rule points down. In the right two panels of Figure 6, we see that velocity dispersion increases closer to the galaxy, while that trend is not visible in the left two panels.

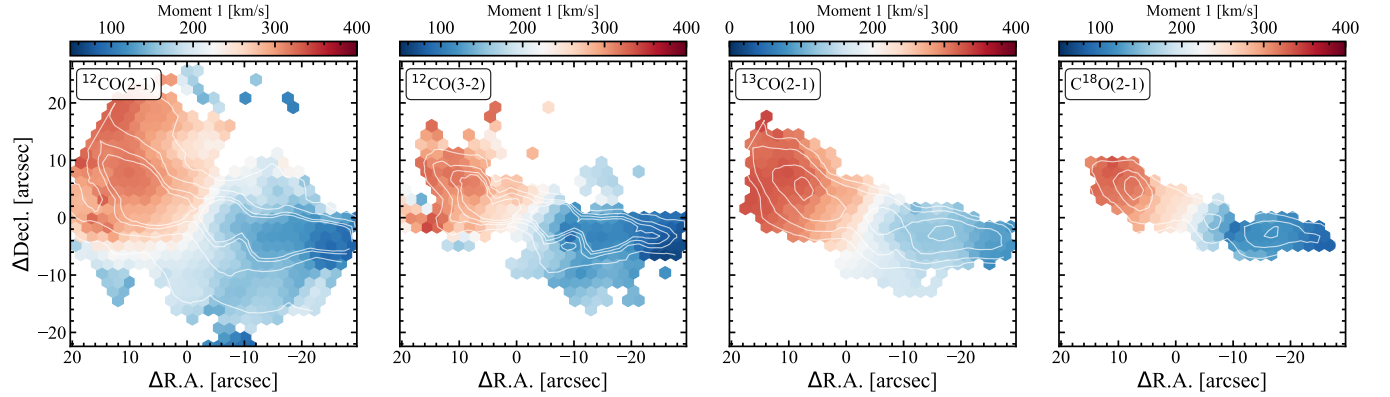


Figure 5. Moment 1 For High Resolution Data.

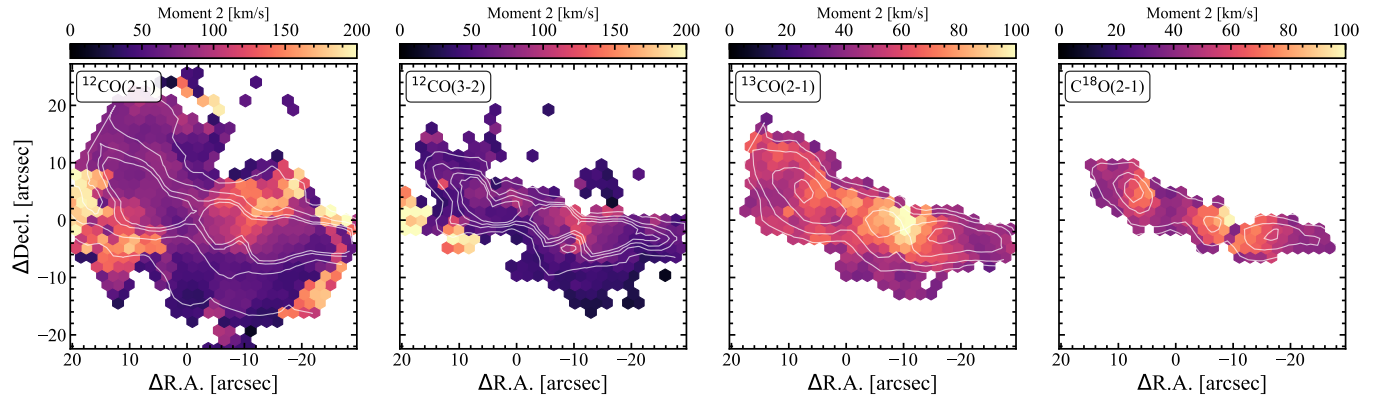


Figure 6. Moment 2 For High Resolution Data.

2.3. Multi-line Non-LTE Modeling Setup

Non local thermal equilibrium radiative transfer code RADEX calculates the intensities of molecular lines based on statistical equilibrium calculations involving collisional and radiative processes (van der Tak et al. 2007). One of the equations governing the calculations in RADEX is the radiative transfer equation (RTE), which describes how an intensity changes as it propagates through a medium of path ds ;

$$\frac{dI_\nu}{ds} = j_\nu - \kappa_\nu I_\nu. \quad (1)$$

In Equation 1, j_ν is the emission coefficient and describes the increase of radiation while κ_ν is the absorption coefficient and describes the decrease of radiation. These coefficients are further governed by other constants and values such as the Einstein A coefficients and physical conditions of the gas, which we input to RADEX.

In this paper, we use RADEX to simulate line intensities and to constrain the density of H_2 (n_{H_2} , also referred to as n_0), kinetic temperature (T_{kin}), and CO column density per line width ($N_{\text{CO}}/\Delta v$), and later, a distribution width σ . As mentioned previously, we construct three models, each following a different formalism. The first assumes a one-component gas phase, the second assumes a log-normal density distribution, and the third assumes a novel log-normal temperature distribution.

RADEX inputs require a molecular data file that includes the energy levels, statistical weights, Einstein A coefficients, and collisional rate coefficients of each molecule. We use the CO, ^{13}CO , and C^{18}O data files from the Leiden Atomic and Molecular Database (Schöier et al. 2005). We create an input file by directly loading in varying values of n_{H_2} , T_{kin} , and N_{CO} . We assume that the CO isotopologues will only collide with H_2 because of its high abundance. Each set of physical parameters uniquely determines a set of modeled line intensities and ratios. We first run RADEX three times (once for each isotopologue) to build a grid with intensity values of all relevant transitions. As listed in Table 3, the model runs through a three dimensional space with $\log n_{\text{H}_2}$ varied from -2 to 9 in steps of 0.167 dex, T_{kin} varied from 3 to 120 K in linear steps of 1 K, and $\log(N_{\text{CO}}/\Delta v)$ varied from 14 to 19 in steps of 0.33 dex (Note that we vary $\log n_{\text{H}_2}$ and T_{kin} to rather low values so that our later implementation of density and temperature distributions in 2.3.1 and 2.3.2 can be finer and therefore more accurate). Other conditions are fixed, such as the abundance ratios $\text{CO}/^{13}\text{CO}$ ($X_{12/13}$) and $^{13}\text{CO}/\text{C}^{18}\text{O}$ ($X_{13/18}$). $X_{12/13}$ was chosen to be 50 and $X_{13/18}$ was chosen as 4 to reflect the environment of M82's galactic center and to align with previous studies of starburst galaxies (Meier et al. 2001; Langer & Penzias 1990; Wouterloot et al. 2008). Other relevant initial conditions are detailed in Table 3, and all RADEX grids in this paper use this grid as a base unless otherwise noted.

Table 3. Summary of One-Zone Gas Phase Initial Conditions

Parameter	Range	Stepsize
$\log(n_{\text{H}_2} [\text{cm}^{-3}])$	-2.0 – 9.0	0.167 dex
$T_{\text{kin}} [\text{K}]$	3.0 – 120.0	1
$\log(N_{\text{CO}} [\text{cm}^{-2}])$	13.0 – 18.0	0.33 dex
$X_{12/13}$	50	...
$X_{13/18}$	4	...
$\Delta v [\text{kms}^{-1}]$	10	...

2.3.1. Incorporating a Log-Normal Density Distribution

Theoretical and observational studies have revealed that molecular clouds have a wide range of gas densities from diffuse to dense ones (Nishimura et al. 2019). Therefore, a one zone model is not sophisticated enough to accurately capture the physical characteristics gas. Also, a sophisticated model is further supported by previous studies of M82, which revealed inconsistencies and difficulties of other models (Mao et al. 2000). To model the molecular gas more physically, we implement a sophisticated log-normal distribution for the density of H_2 , the first implementation such a model to M82. We follow formulations that model the density distribution of a turbulent cloud. We adopt the probability density function (PDF) method used in Leroy et al. (2017) and implement it for our RADEX grid. In the Padoan & Nordlund (2002) formulation, the gas volume density in a cloud can be described by

$$dP(\ln n') \propto \exp\left(-\frac{(\ln n' - \overline{\ln n'})^2}{2\sigma^2}\right) d(\ln n'), \quad (2)$$

where dP is the fraction of molecules with volume densities in a logarithmic step $d \ln n'$ centered on n' , $n' = n_{\text{H}_2}/n_0$ is the volume density, and σ is the width of the distribution. Note that the distribution does not peak at the center volume density (n_0), but rather it peaks at $\ln n'$. This can be seen in Figure 7, where we plot density distributions for two distribution widths. Similar to Leroy et al. (2017), we work in \log_{10} instead of \ln , so our σ differ from the Padoan & Nordlund (2002) formulation by a factor of $\ln 10$.

To implement this density distribution, we adopt the equation used in Leroy et al. (2017) to recalculate the intensities by considering a PDF of densities $P(n_{\text{H}_2})$ and integrating over each density n_{H_2} . We take our grid produced from 2.3 and isolate rows with more reasonable $\log n_{\text{H}_2}$ values from 2 to 7 to account for distribution width (if we were to perform this calculation for $\log n_{\text{H}_2} = -2$, we would encounter the issue of not having intensity values for even smaller densities). For each row, we iterate over σ values ranging from 0.1 to 0.9 in steps of 0.1 and calculate I_{density} as follows. We have

$$I_{\text{density}} = \frac{\int n_{\text{H}_2} P(n_{\text{H}_2}) I(n_{\text{H}_2}, N_{\text{CO}}, T_{\text{kin}}) dn_{\text{H}_2}}{\int n_{\text{H}_2} P(n_{\text{H}_2}) dn_{\text{H}_2}}, \quad (3)$$

where for each row with $\log n_{\text{H}_2}$ value from 2 to 7, we fix the T_{kin} and $N_{\text{CO}}/\Delta v$ value and evaluate Equation 3 over the entire grid from 2.3. The parameters in which we implement this density distribution for are detailed in Table 4.

Table 4. Summary of Density Distribution Implementation.

Parameters	Range	Step Size
$\log(n_{\text{H}_2} [\text{cm}^{-3}])$	2.0 – 7.0	0.167
$T_{\text{kin}} [\text{K}]$	3.0 – 120.0	1
σ	0.1 – 0.9	0.1

2.3.2. Incorporating a Log-Normal Temperature Distribution

The variation of temperature in turbulent clouds is often ignored. As a result, efforts to develop models to prescribe temperature are overshadowed. In the modeling of molecular gas, the temperature is either assumed to be constant or assumed to be half hot and half cold (Teng et al. 2022). These assumptions neglect that temperature can vary on small scales.

We therefore introduce a novel implementation of a log-normal temperature distribution. The temperature of a molecular cloud varies as well, and therefore, an assumption of a singular temperature can be improved upon. Similar to the log-normal in 2.3.1, we implement a log-normal temperature distribution and follow Equation 2. However, because temperatures are significantly closer in dex and take steps in linear space, we use smaller distribution widths σ from 0.01 to 0.09 in steps of 0.01. The smaller scale of temperatures makes for a sensitive probability function. As shown in Figure 7, small changes in σ influence the PDFs of density and temperature significantly.

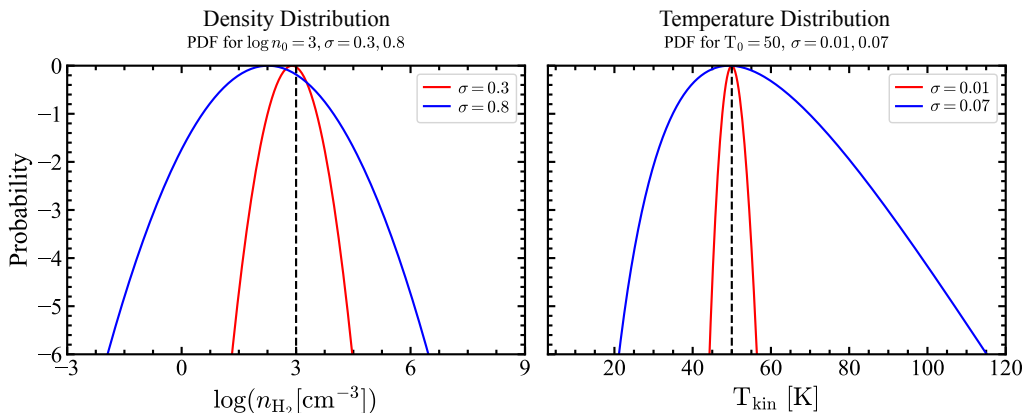


Figure 7. Density and Temperature Distributions for $\sigma = 0.3, 0.8$, and $\sigma = 0.01, 0.07$ respectively. We plot the density PDF in log scale with $n_0 = 3$ as a function of $\log n_{\text{H}_2}$. We plot the temperature PDF in similar log scale with $T_0 = 50\text{K}$ as a function of T_{kin} .

To recalculate intensities, we have

$$I_{\text{temp}} = \frac{\int T_{\text{kin}} P(T_{\text{kin}}) I(n_{\text{H}_2}, N_{\text{CO}}, T_{\text{kin}}) dT_{\text{kin}}}{\int T_{\text{kin}} P(T_{\text{kin}}) dT_{\text{kin}}}, \quad (4)$$

where $P(T_{\text{kin}})$ is the probability density function for temperature and $I(n_{\text{H}_2}, N_{\text{CO}}, T_{\text{kin}})$ is the simulated intensity value given a set of parameters. We perform this calculation only for rows with T_{kin} between 10 and 80 K (to account for distribution width). The parameters in which we implement this temperature distribution for are detailed in Table 5.

Table 5. Summary of Temperature Distribution Implementation.

Parameters	Range	Step Size
T_{kin} [K]	10.0 – 80.0	1
$\log(n_{\text{H}_2} [\text{cm}^{-3}])$	2.0 – 7.0	0.167
σ	0.01 – 0.09	0.01

Because the specific impacts of a log-normal distribution is complex, we created an interactive tool for visualization and educational purposes. The tool allows users to see the complex interplay between input parameters and simulated line ratios. Refer to B for more details.

2.4. RADEX Fitting

After forming a grid of simulated intensities, we must fit our observed data to the models. We adopt the Bayesian maximum likelihood analysis used in Teng et al. (2022) to constrain the distributions of gas parameters including n_{H_2} , T_{kin} , and N_{CO} .

For one zone modeling, we fit the 107 pixels in the high resolution map of moment 2 (Figure 6) by using our RADEX grid of intensities and ratios and comparing it to observed ratios. To evaluate the quality of fit for each set of initial conditions $\theta = (n_{\text{H}_2}, T_{\text{kin}}, N_{\text{CO}})$ from Table 3, we compute the χ^2 values at each point in the model grid:

$$\chi^2(\theta) = \sum_{i=1}^n \frac{[R_i^{\text{model}}(\theta) - R_i^{\text{obs}}]^2}{\sigma_i^2}, \quad (5)$$

where R^{model} and R^{obs} are the modeled and observed ratios of line integrated intensities. σ_i is the uncertainty of the ratios we fit for, calculated by propagating the error of each line intensity. For every pixel, we introduce a minimum σ_i of 10% of the ratio itself (ie, if the propagated σ is less than 10% of the ratio itself, we set the σ equal to 10%). For one zone modeling, $n = 3$ because we fit for three line ratios (and three parameters). Specifically, we fit for the $^{12}\text{CO}(3-2)/^{12}\text{CO}(2-1)$ ratio, the $^{13}\text{CO}(2-1)/^{12}\text{CO}(2-1)$ ratio, and the $\text{C}^{18}\text{O}(2-1)/^{12}\text{CO}(2-1)$ ratio. These ratios each trace a different condition, which is explained further in 3.1. We note that because we are fitting for three free parameters, fitting for three ratios suffices. As in Teng et al. (2022), we assume a multivariate Gaussian probability distribution and we convert the χ^2 value to a probability. We have

$$P(R^{\text{obs}} | \theta) = \frac{1}{Q} \exp\left[-\frac{1}{2}\chi^2(\theta)\right], \quad (6)$$

where $Q^2 = \prod_i (2\pi\sigma_i)$. For every point in our simulated parameter space, we calculate the probability associated with it. We then reshape our probabilities into a cube and generate the marginalized 1D and 2D distributions. These distributions are calculated by summing along axes of the cube (in other words, we collapse the cube down to either 2D or 1D by summing along axes). We then visualize our results in 3.3.

For the log-normal modeling, we follow the same procedure as above except calculate all necessary values from the grid of recalculated intensities and fit for four parameters rather than three (distribution width σ , this σ different than propagated error being the new parameter). Because the implementation of a distribution width introduces a new degree of freedom, we must fit for at least 4 ratios, which requires the use of the low resolution data because we only have four high resolution line intensities and cannot avoid degeneracies. While using low resolution data for analysis means we can only determine physical parameters on a larger scale, analysis of line ratios in Figure 8 demonstrates

variation in conditions even in kpc scale. Because of the larger scale, we must fit for less pixels. Specifically, we fit for the 23 pixels in which moment 2 of $^{13}\text{CO}(2-1)$ is defined. Moment maps can be found in the A.

For both distributions, we fit for the following four ratios: $^{12}\text{CO}(3-2)/^{12}\text{CO}(2-1)$, $^{13}\text{CO}(2-1)/^{12}\text{CO}(2-1)$, $^{12}\text{CO}(2-1)/^{12}\text{CO}(1-0)$, and $^{13}\text{CO}(1-0)/^{12}\text{CO}(1-0)$. We use the same equations and methods used above for one zone modeling, except now $n = 4$ because we fit for four ratios. Similar calculations of 1D and 2D distributions were performed. Following calculations of 1D and 2D distribution, we can then calculate fitted values for each parameter, which is described further in 3.3.

3. RESULTS AND ANALYSIS

3.1. Line Ratios at Kiloparsec Scale

Figure 8 shows the low resolution $^{13}\text{CO}(2-1):^{12}\text{CO}(2-1)$ and $^{12}\text{CO}(3-2):^{12}\text{CO}(1-0)$ ratios. On the left panel, we only display pixels with $S/N > 2.5$ for both lines and on the right panel, we only display pixels with $S/N > 5$ for both lines. Assuming that ^{13}CO abundance does not change, the ratio in the left panel traces the optical depth of ^{12}CO optical depth since ^{13}CO is optically thin (den Brok 2022). We see in the left panel that the ratio peaks at the center of the galaxy (when the difference in right ascension and declination measured from the center is 0) and tapers off as a function of distance from center. Assuming the variation is driven purely by opacity, this implies that the gas becomes more optically thick closer to the center. Davis (2014) suggests that the physical drivers of increasing optical depth changes could be a result of changing temperature and velocity dispersion. However, the ratio is likely also affected by changes in relative abundance. Regardless, the variation in ratio indicates some form of changing parameters in kpc scale.

On the right panel of Figure 8, we show a ratio between different transitions of the same molecule. This ratio traces excitation conditions of the CO gas, which is linked to changes in T_{kin} and n_{H_2} (Shirley 2015). By comparing the intensity of one energy line transition to another, we effectively are looking at how much of the gas is in an excited energy state, which is governed by T_{kin} and n_{H_2} . We see in the right panel that regions closer to the center of the galaxy have a higher ratio. This demonstrates that there is variation in T_{kin} and n_{H_2} throughout the galaxy, specifically that the center of the galaxy must have higher T_{kin} and/or higher n_{H_2} than the rest of the galaxy. It is important to note that our conclusions here can only be made on a kiloparsec scale because we use low resolution data.

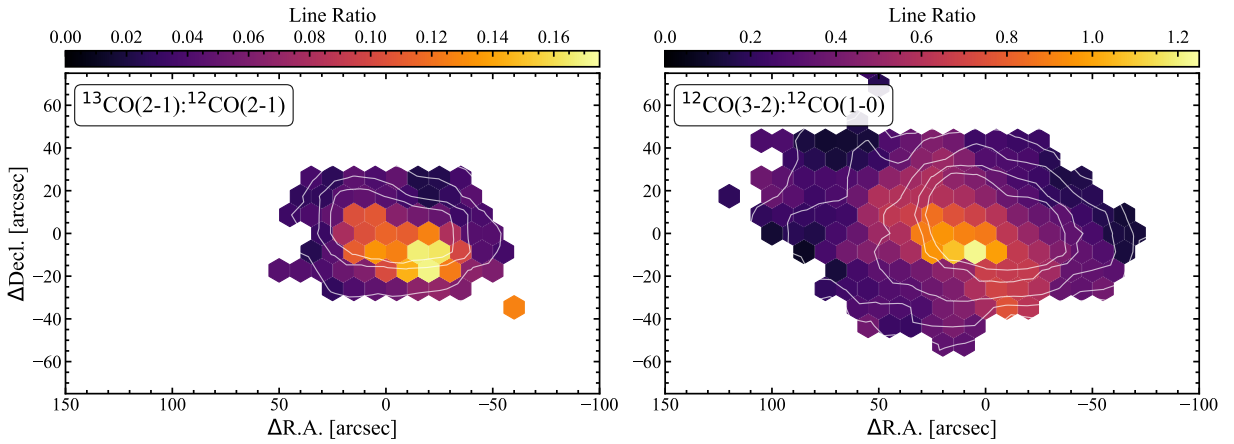


Figure 8. $^{13}\text{CO}(2-1):^{12}\text{CO}(2-1)$ and $^{12}\text{CO}(3-2):^{12}\text{CO}(1-0)$ ratios from the low resolution data cube. We plot contours of the integrated intensity of $^{12}\text{CO}(2-1)$ on the left and contours of the integrated intensity of $^{12}\text{CO}(1-0)$ on the right. We only plot the ratio for pixels satisfying a benchmark S/N ratio of 2.5 and 5, respectively.

Figure 9 plots the $^{12}\text{CO}(2-1):^{12}\text{CO}(1-0)$ against the galactocentric radius. Similar to Figure 8, we only display points with $S/N > 5$ for both $^{12}\text{CO}(2-1)$ and $^{12}\text{CO}(1-0)$. As mentioned above, the ratio of two different energy transitions for the same molecule traces excitation conditions. In this figure, we see a general downward trend as we move farther away from the center of the galaxy, which aligns with what we saw in Figure 8. This means that either T_{kin} or n_{H_2} (or both) must decrease as we move away from the center. We also see that a higher intensity of $^{12}\text{CO}(1-0)$ corresponds to a higher ratio.

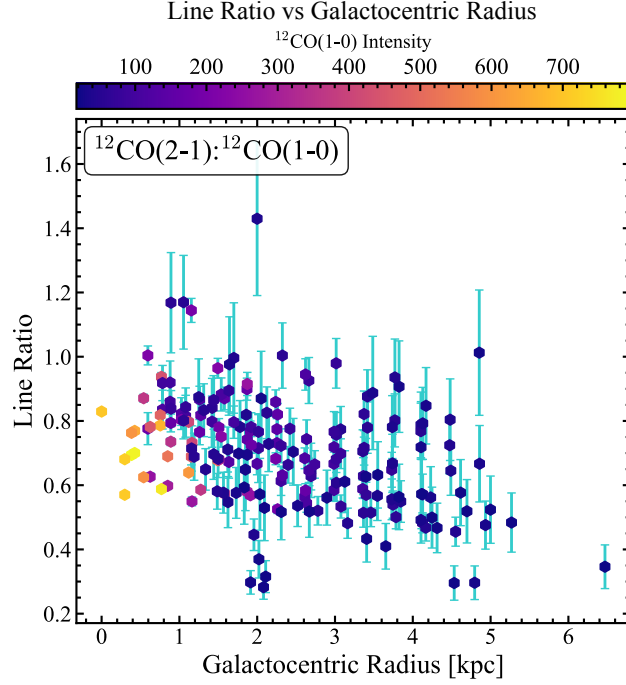


Figure 9. $^{12}\text{CO}(2-1):^{12}\text{CO}(1-0)$ ratio plotted against galactocentric radius in units of kpc. We color each point by the intensity of the $^{12}\text{CO}(1-0)$ line and include error bars corresponding to the ratio.

3.2. High Resolution Line Ratios

From 3.1, we saw variance in line ratios in kpc scale. We now investigate for variance in high resolution ratios. Moment maps in Figure 4 show three bright regions. Figure 10 defines the three regions using the $\text{C}^{18}\text{O}(2-1)$ moment 0 map first shown in Figure 4. Region 2 is spherical and is ~ 4 pixels in diameter, and because the pixels are half beam sized, this corresponds to a distance of ~ 120 pc. Note, these regions are not directly at the center of the galaxy.

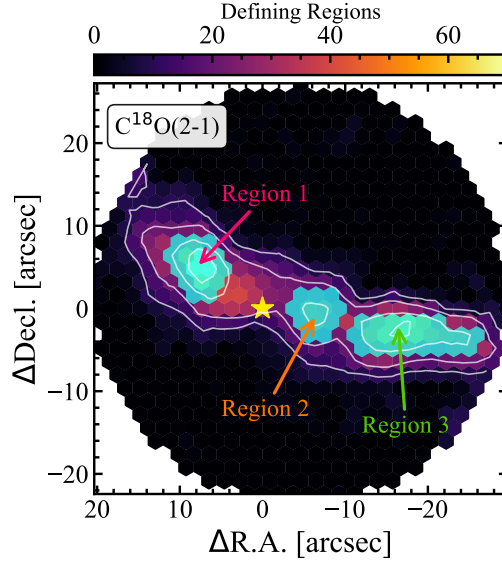


Figure 10. Defining three regions from $\text{C}^{18}\text{O}(2-1)$ moment 0 map. Each region corresponds to a different color (region 1 is pink, region 2 is orange, and region 3 is green) and is defined by cyan. The yellow star marks the center of the galaxy determined by Jackson et al. (2007).

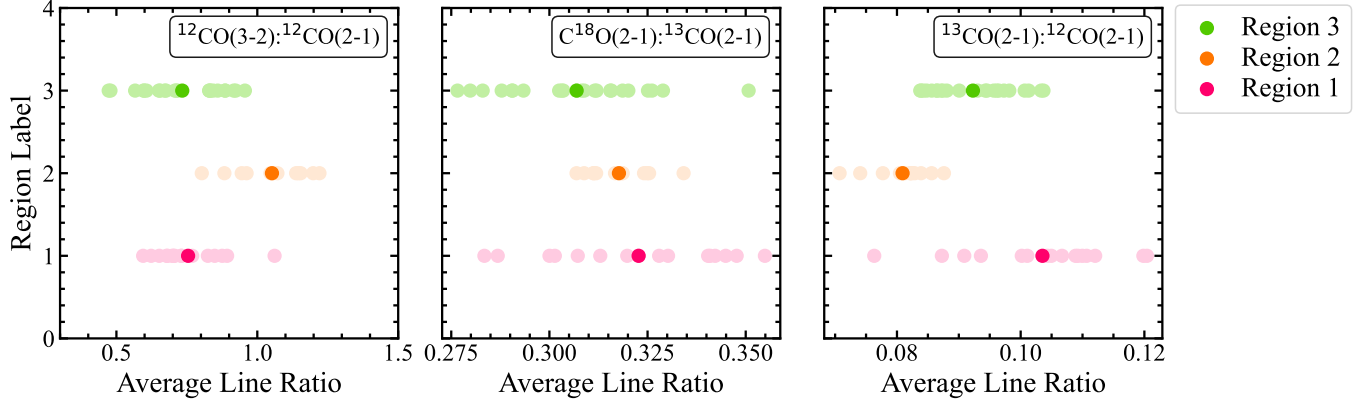


Figure 11. $^{12}\text{CO}(3-2):^{12}\text{CO}(2-1)$ ratio, $\text{C}^{18}\text{O}(2-1):^{13}\text{CO}(2-1)$ ratio, and $^{13}\text{CO}(2-1):^{12}\text{CO}(2-1)$ ratio plotted and averaged for each region. The x-axis is the line ratio and the y-axis corresponds to the region label.

Figure 11 shows three line ratios for each region. In the leftmost panel, we show the $^{12}\text{CO}(3-2):^{12}\text{CO}(2-1)$ ratio; in the middle panel, we show the $\text{C}^{18}\text{O}(2-1):^{13}\text{CO}(2-1)$ ratio; in the rightmost panel, we show the $^{13}\text{CO}(2-1):^{12}\text{CO}(2-1)$ ratio. We plot the average line ratio for each region in the brightest color and denote the scatter in a lighter color. The leftmost panel displays a ratio between two energy transitions for the same molecule and therefore traces excitation conditions, as first mentioned in 3.1. We see that Region 2, which is the region closest to the center of the galaxy, has an average ratio around 25% higher than Region 1 and 3 (note that Region 2 is not exactly at the center of the galaxy; it is displaced to the right). This demonstrates the drastic variation in T_{kin} and/or n_{H_2} near the center of the galaxy. One important note is that we saw this similar variation even in kpc scale in 3.1, and we see a similar variation even in much finer scale.

The middle panel of Figure 11 shows a ratio between two optically thin emission lines. This ratio helps us constrain any changes in relative abundances of the species. We see that the regions seem to have a linear increase (as seen if we move from Region 1 to 3), with Region 2’s ratio being within 1% of the average of Region 1 and Region 3. This suggests a change in fractional abundance of C^{18}O and ^{13}CO , which can be driven by multiple processes such as selective photodissociation, and selective nucleosynthesis (Davis 2014).

Finally, the rightmost panel of Figure 11 traces variance in optical depth. We compare $^{13}\text{CO}(2-1)$ and $^{12}\text{CO}(2-1)$, which is a ratio between an optically thin and optically thick isotopologue. In Region 2, the ratio dips down, which is most likely due to optical thinning of $^{12}\text{CO}(2-1)$ because thinner ^{12}CO enhances the emission as we probe deeper into the cloud. As mentioned in 3.1, changes in optical depth could be driven by temperature or velocity dispersion. The ratio could also be driven by changes in relative abundances of ^{13}CO , but because there is not significant variance in $\text{C}^{18}\text{O}/^{13}\text{C}$, we can exclude this explanation. Determining the specific driver of such changes is beyond the scope of this paper, but the variance in ratio reveals motivation to further analyze conditions of the center.

Analyzing high resolution and low resolution line ratios reveals variance in molecular gas conditions throughout the center of M82. Specifically, we see extreme excitation conditions closer to the center of the galaxy and some variance in relative abundance. While high resolution and low resolution demonstrate contrasting results in ratios that trace optical depth, they still demonstrate variance in the center of the galaxy that must be studied further. With our analysis, we can use non-LTE simulations to model our data and see whether or not our the inferred values match our ratio analysis.

3.3. Radex Modeling Results

3.3.1. High Resolution One Zone Modeling Results

Following our Bayesian maximum likelihood analysis outlined in 2.4, we can find the conditions that best reproduced our observed multi-line emission. With our 1D distributions, we find the “maximum fit” for each pixel, which is the specific parameter value that gives the highest 1D likelihood. We also find the “weighted fit” which is the weighted average of the different values of a specific parameter and the 1D distribution probability associated with it.

We visualize fitted results in corner plots which were made for each pixel. The diagonal of the corner plots consist of a probability plot for an individual parameter. Peaks in these demonstrate our fit parameters. The off diagonal of

the corner plots contain scatter plots, which show relationships between two parameters. Figure 12 are corner plots for two bright pixels in the galaxy and show the marginalized likelihood distributions.

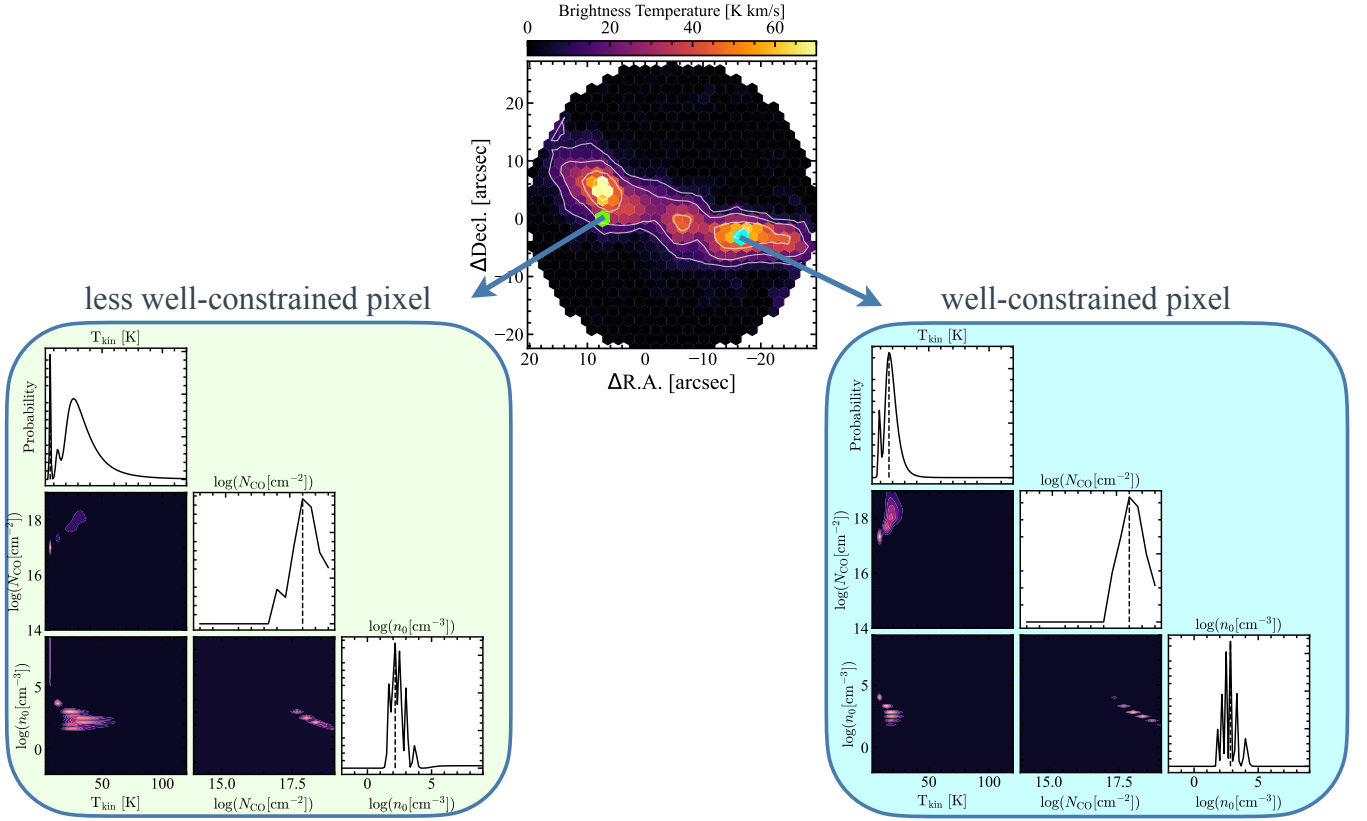


Figure 12. One Component Modeling Corner Plots. The left plot represents a less-well constrained pixel and the right plot represents a well-constrained pixel. In corner plots, the 1D distributions are plotted along the diagonal and the 2D distributions are plotted in the corner.

From left to right, the parameters are T_{kin} , $\log N_{\text{CO}}$, and $\log n_0$. We see distinct peaks in the right panel and sparse and large groups of color in the 2D distributions, while we see less distinct peaks in the left panel and more smaller groups of color in the 2D distributions (the brighter a pixel in a 2D distribution, the higher the probability. This means the appearance of many bright groups of color demonstrates a loosely constrained pixel). We see that for both corner plots, the one zone model infers a peak in probability for a relatively low T_{kin} . For the left panel, the probability for T_{kin} shows a tail distribution towards larger values (see the sharp peak and then another wider peak). This possibly suggests that the original RADEX model needed to be run for an even larger range of temperatures and that the peak in the lower temperature may be misleading. This discrepancy in ability to fit likely is because the left pixel is less bright than the right. The right pixel is also closer to the center of a knot, while the left pixel lies on the edge of a knot (see Figure 10 for defined knots). The general difficulty in fitting is likely because lack of high resolution data. In this case where we only fit for 3 lines, it can be difficult to tightly constrain the parameter set. A summary of all fits can be found in Table 6.

As explained in 1, one zone modeling potentially oversimplifies actual physical behavior in molecular clouds. However, one zone modeling is a good diagnostic and convenient method to build preliminary understanding of the physical conditions of a galaxy. In our case, it provides a benchmark for the comparison to the other multi-line model prescriptions.

3.3.2. Low Resolution Density and Temperature Distribution Modeling Results

Similar to corner plots presented in Figure 12, we make corner plots from calculated fits of log-normal distribution. Figure 13 are corner plots for the same pixel, and the left corner plot shows results from the log-normal density distribution while the right corner plot shows results from the log-normal temperature distribution.

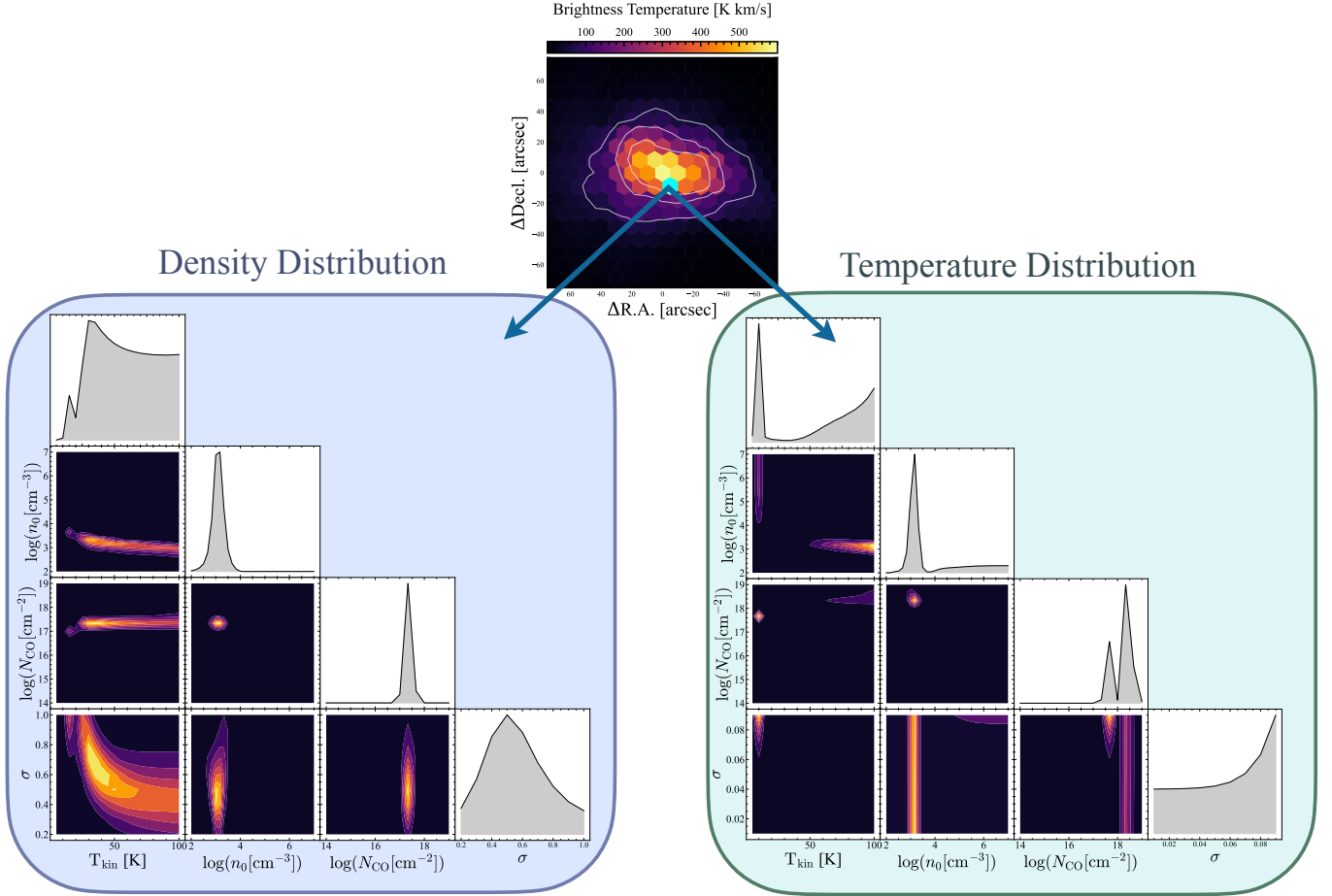


Figure 13. Log-normal Distribution Corner Plots. The left plot is the density distribution corner plot and the right plot is the temperature distribution corner plot.

From left to right, the parameters are T_{kin} , $\log n_0$, $\log N_{\text{CO}}$, and σ . The 1D and 2D distributions are less tightly constrained than in one zone modeling, which could be because the RADEX simulation grid is too coarse and possibly does not cover the parameter space needed to reproduce the observed line ratios. It is also possible that because low resolution data covers a much larger scale and resolves less internal structure, the fits are less robust.

In both corner plots, $\log n_0$ and $\log N_{\text{CO}}$ are the most well constrained parameters, and T_{kin} and σ are the least well constrained. This can be seen from the diagonal plots, as the 1D distribution of temperature has a less pronounced peak. In the right panel (Temperature Distribution corner plot), the temperature has a peak and then dips down, then increasing in hotter conditions (a tail). In the left panel (Density Distribution corner plot), the temperature has a wide peak and does not dip down. For σ , both plots demonstrate that the distribution width indeed affects the probability drastically, meaning that the implementation still makes a significant difference. However, both models are unable to constrain σ well in one defined peak, and as a result, we consider the weighted fit rather than the maximum fit. For the density distribution, we find the following: the average maximum $T_{\text{kin}} = 65.43$ K, the average weighted $\log N_{\text{CO}} = 18.12$, the average weighted $\log n_0 = 3.15$, and the average maximum $\sigma = 0.71$. For the temperature distribution, we find the following: the average weighted $T_{\text{kin}} = 67.56$ K, the average weighted $\log N_{\text{CO}} = 18.10$, the average maximum $\log n_0 = 3.24$, and the average maximum $\sigma = 0.089$. The averaged results from the distribution models and one zone models are summarized in Table 6.

Table 6. Summary of results from RADEX modeling. Avg Max refers to the averaged maximum fit and Avg Weighted refers to the averaged weighted fit.

Parameter		One Zone	Density Distribution	Temperature Distribution
T_{kin} [K]	Avg Max	38.99	65.43	75.65
	Avg Weighted	63.86	61.47	67.56
$\log(N_{\text{CO}} [\text{cm}^{-2}])$	Avg Max	18.36	18.15	18.09
	Avg Weighted	18.29	18.12	18.10
$\log(n_{\text{H}_2} [\text{cm}^{-3}])$	Avg Max	3.95	3.12	3.24
	Avg Weighted	5.60	3.15	2.88
σ	Avg Max	...	0.71	0.089
	Avg Weighted	...	0.80	0.052

To interpret values from log-normal fits, we plot the distributions that our results predict in log scale. Figure 14 uses values from Table 6. In the left panel, we plot the density distribution and in the right panel, we plot the temperature distribution. In the right panel, we see how it seems like the temperature distribution leans closer to the right, i.e. closer to higher temperatures.

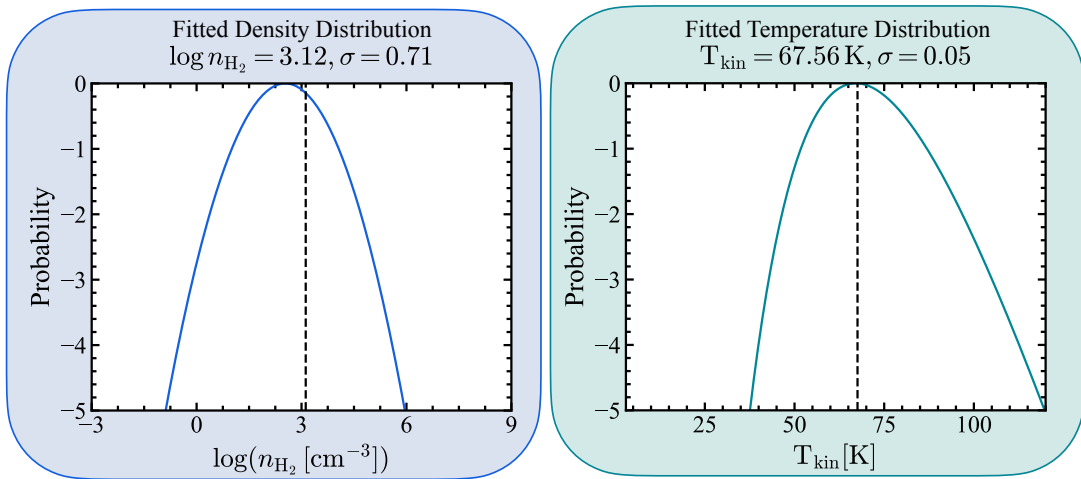


Figure 14. Density and Temperature distributions. Each distribution uses best fit parameters summarized in Table 6.

3.3.3. Analysis, Variation, and Comparison of Fitted Parameters

To see how our fitted results align with previous line ratio analysis from 3.1 and to see how the two models differ from one another, we show color maps in Figure 15.

The colormaps plot the weighted fits of each parameter for each log-normal model, with the log-normal density on top and the log-normal temperature model on the bottom. All colormap scales are identical with the exception of σ .

As mentioned in 3.1, we expect that the regions closest to the center of the galaxy should have more extreme excitation conditions (i.e. hotter and/or denser gas) because of higher $^{12}\text{CO}(3-2)/^{12}\text{CO}(1-0)$ ratio. Furthermore, high resolution Figures 10 and 11 showed that the exact center of the galaxy did not have the highest ratios. Rather, the region to the right of the center exhibited the highest $^{12}\text{CO}(3-2)/^{12}\text{CO}(2-1)$ ratio. Looking to the log-normal density map fit, i.e. the top panel of Figure 15, we see the temperature or density does not seem to increase significantly to the right of the center. In fact, in the $\log n_0$ plot, there is a region of very low density. However, in this same region, σ peaks, which means the PDF is wider and larger densities have higher probabilities. This could give an effect of a higher density. This also reveals a possible degeneracy in fitted $\log n_0$ values and σ values, because more extreme excitation conditions could be reached by either larger $\log n_0$ or a larger σ . Looking at the log-normal temperature map fit, we similarly do not see a significant increase in temperature or density to the right of the center. However, there is one pixel to the right of the center with extreme σ , which similarly gives the effect of a higher temperature.

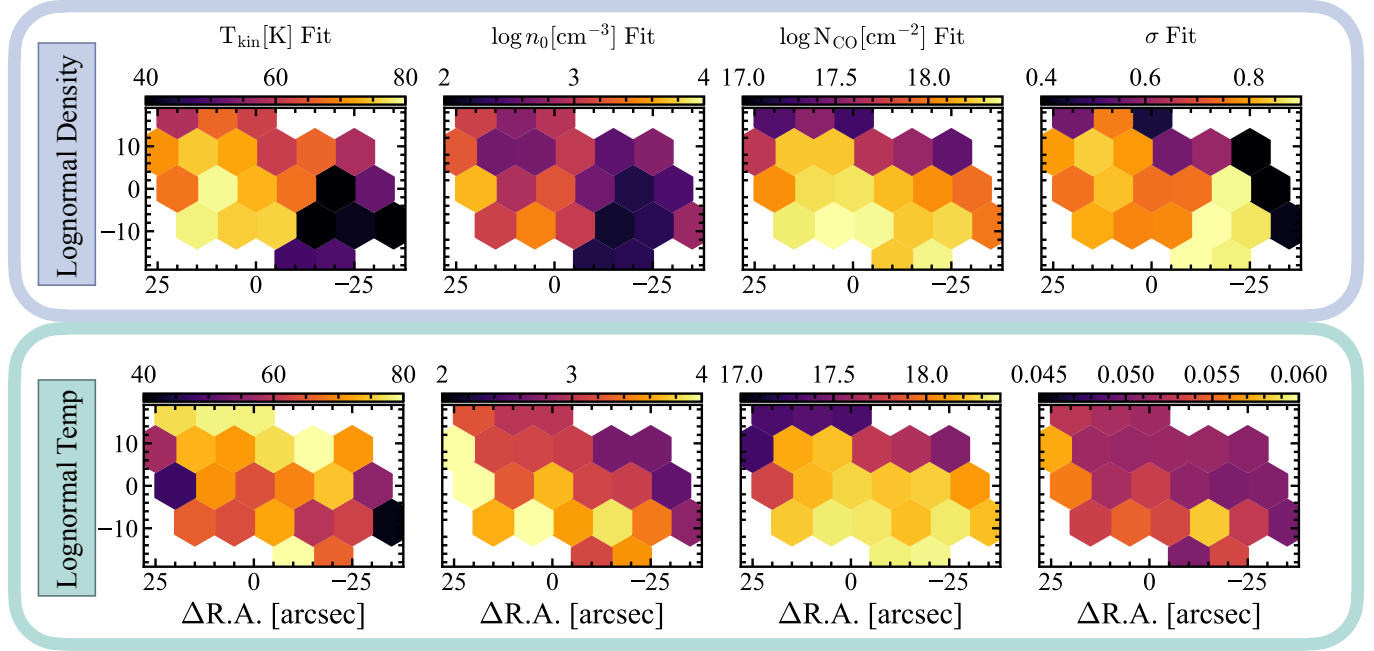


Figure 15. Log-normal Density and Temperature Result maps. The colormap scales are the same for each parameter with the exception of σ . The top panel is the log-normal density model and the bottom panel is the log-normal temperature model. The y axis is declination and the x axis is right ascension.

It seems that there is a degeneracy between distribution width and the parameter that is changing. Still, results from log-normal models align with what we expect from line ratio analysis. Avoiding this degeneracy could likely be done by constraining with more ratios or by extending the initial RADEX grid to even higher densities and temperatures.

Now, we compare how the maps differ from one another. The two models generally agree regarding T_{kin} , with the exception of a dark pixels in the log-normal density fit. The two models generally seem to agree for the fit of $\log n_0$. They both identify similar values in the top region. In the lower region, the log-normal density fit predicts lower densities, but we also must keep in mind that each density has a distribution width attached to it, which gives the effect of a smoothly changing density and possibly the effect of a larger density. The two models demonstrate very similar results for $\log N_{\text{CO}}$, down to how the column density varies across the galaxy as well. While we cannot directly compare the σ because they represent the distribution width of two different parameters, we can discuss their variance. We see that the log-normal temp model predicts a virtually constant distribution width while the log-normal density fit predicts a distribution that varies more across the central region. Further research is needed to explain the specific behavior of σ .

Finally, we compare the three models with one another, specifically their final averaged results summarized in Table 6. We compare by using percentage difference between Avg Max and Avg Weighted yields. We see that the two log-normal models generally agree with one another and both contrast the most with the one zone model. The one zone model predicts a lower Avg Max T_{kin} by 40% when compared to the Density Distribution and by 48% when compared to the Temperature Distribution. Unsurprisingly, the log-normal models disagree most significantly on T_{kin} and $\log n_{\text{H}_2}$, with the Temperature Distribution deriving a higher T_{kin} by 16% when comparing the Avg Max and by 10% when comparing the Avg Weighted. From Table 6, we see that generally the log-normal temperature fit predicts a higher T_{kin} fit than both other models and a lower Avg Weighted $\log n_{\text{H}_2}$ than both other models. The Temperature Distribution inferred Avg Weighted $\log n_{\text{H}_2}$ is less than the other Avg Weighted fits by 48% (one zone) and by 9% (density distribution). We see that $\log N_{\text{CO}}$ seems to not be affected by implementations of new models, with all values of $\log N_{\text{CO}}$ within 1.5% of each other.

3.4. LTE Modeling

As a further attempt to benchmark the results from multi-line non-LTE models, we compare results from 3.3 to results from calculations that assume the gas is in LTE. While one zone modeling possibly simplifies the reality of molecular clouds, in our case, the results are a good benchmark for comparison.

Using high resolution data, we use equations from (Nishimura et al. 2015) to calculate excitation temperatures of $^{12}\text{CO}(2-1)$ and $^{13}\text{CO}(3-2)$. The equations can be found in C. Figure 16 plots the $^{12}\text{CO}(3-2)$ and $^{12}\text{CO}(2-1)$ excitation temperatures against each other. If the molecular gas truly is in LTE, then the calculated excitation temperatures should be equal. We see that the calculation temperatures fit relatively well to the $y = x$ line. We perform a linear fit for the data and account for error in intensity by perturbing the intensity value, recalculating the excitation temperatures, and refitting the line. We yield a fit of $m = 0.935$ and $b = 2.051$, where the general form of the line is $y = mx + b$. The general agreement of the two temperatures, and the linear fit slope of $m = 0.935$ demonstrate that an assumption of LTE is not necessarily incorrect. LTE may be an accurate representation of M82's molecular gas.

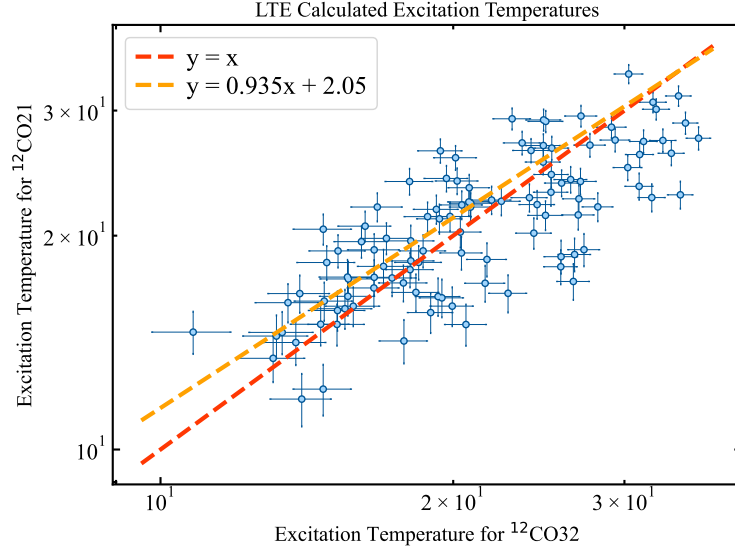


Figure 16. Calculated $^{12}\text{CO}(3-2)$ and $^{12}\text{CO}(2-1)$ excitation temperatures under LTE assumption. We plot in red the $y = x$ line and plot in orange the average fit. In blue, we plot the errorbars.

We compare LTE calculated column densities with one zone modeled column densities in Figure 17. For each of the 107 pixels with a one zone column density fit, we calculate the column density under the assumption of LTE using equations in C. In Figure 17, we plot the LTE calculations in blue and the RADEX fit in yellow. We see that the LTE column densities are greater than the RADEX fit by around 0.2 dex and share a common region of 0.6 dex.

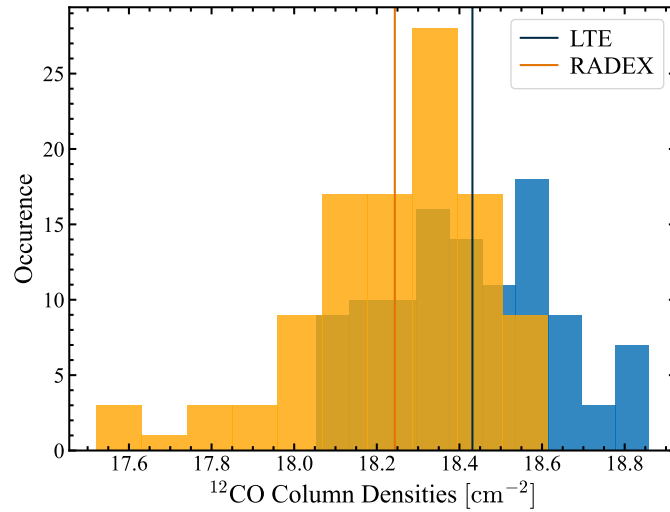


Figure 17. LTE and RADEX ^{12}CO column densities. We show RADEX in yellow and LTE in blue.

4. DISCUSSION

Analysis of high resolution and low resolution line ratios between optically thick and thin lines reveal variation in excitation conditions, relative abundance, and optical depth across the central molecular zone of M82. We see generally more extreme excitation conditions in regions closest to the center and to the right of the center.

Our multi-line modeling under the assumption of a one component and log-normal distribution gas results in different derived environmental parameters. Overall, our log-normal models predict similar results but one zone modeling predicts drastically different results. Specific percentages can be found in 3.3.3 but are summarized here. Log-normal models predict a higher T_{kin} between the range of 61 - 76 K, while the one zone Avg Max is ~ 39 K, which is between 36% and 49% lower. The log-normal models predict a lower $\log n_{\text{H}_2}$ value between 2.88 and 3.24, while the one zone predicts values between roughly 4 and 5.5, which is 30% to 70% higher. There could be a degeneracy in our analysis between T_{kin} and $\log n_{\text{H}_2}$ because an increase in either effects excitation conditions, which governs the ratios that we fit for. Specifically, we see that the temperature distribution model generally predicts higher temperatures but lower densities compared to the density distribution. This degeneracy could possibly be avoided by fitting for more ratios. In terms of $\log N_{\text{CO}}$, our three models generally agree and predict a value of between 18.09 – 18.36.

We compare our results to those in literature. Mao et al. (2000) studied molecular line emission of CO up to a high energy transition of $J = 7 - 6$, meaning they can trace higher temperatures. Their extensive study found a T_{kin} between 60 – 130 K, which our models also predict with the exception of the one zone Avg Max fit. The one zone Avg Max fit is 35% lower than the lowest temperature in that range. Ward et al. (2003) performed a similar extensive study of M82 with higher energy transitions using detailed two component modeling. Ward et al. (2003) found a density ($\log n_{\text{H}_2}$) between 2.4 – 5.0, which our log-normal results fit well into. Our one zone model, however, predicts a $\log n_{\text{H}_2}$ larger than this range by 12%. Ward et al. (2003) also found a T_{kin} greater than 50K and even up to 170K, which our results fit well into with the exception of the one zone Avg Max fit. Overall, results in literature align well with the results from log-normal models and supports the implementation of log-normal models.

To further evaluate the goodness of each model, we must turn to other tracers of molecular gas that do not require assumptions of the state of the gas so as to avoid bias. These studies do not utilize low J CO isotopologue transitions or RADEX. Weiß et al. (2001) uses ammonia (NH_3) as a tracer of molecular gas in M82. Using radiative transfer calculations to calculate T_{kin} , they find that in the center of M82, $T_{\text{kin}} \sim 80$ K. They do not trace any other physical parameters of the gas. Their derived temperature is just $\sim 6\%$ higher than our Avg Max temperature log-normal model, but is more than double that of our Avg Max one zone model. Seaquist & Frayer (2000) is another study that does not use CO as a tracer for molecular gas. Instead, they use HCO+ and HCN emission lines and find that $T_{\text{kin}} \sim 50$ K, which is slightly lower than our general results. Because HCO+ and HCN are excited at low temperatures, it is possible that emission from HCO+ and HCN cannot trace higher temperature. Regardless, results from Seaquist & Frayer (2000) align best with our one zone Avg Max model.

Overall, studying molecular gas requires consideration of a broad spectrum of parameters such as density and temperature. Implementations of a smoothly changing temperature or distribution result in drastically different results from one zone models, as our results have shown. To date, most molecular gas modeling employ a one zone or two zone phase. To take further steps in modeling molecular gas and unraveling its relationship with star formation and galaxy evolution, line emission must be modeled more accurately by considering realistic parameter distributions. Our work clearly suggests that implementing novel log-normal models results in significant differences of the derived physical properties.

Our models, while sophisticated and novel, still have room for improvement. Our current models do not account for changes in the relative abundance of the CO isotopologue species. Further investigation is still needed in the field of developing accurate temperature models. An open question remains: what other methods can we use to constrain the physical parameters of molecular gas in the ISM? Other tracers of molecular gas do exist, and more extensive modeling will contribute to improving multi-line modeling. More computational resources need to be allocated to achieve a finer multi-line modeling grid. At the moment, far infrared observations are limited in angular resolution to $\sim 20''$. New space-based telescopes are required to observe higher energy transitions of CO isotopologues. Regarding the missing $J = 1 - 0$ high resolution data, collaboration efforts are planned with the PIs of Institut de radioastronomie millimétrique’s Northern Extended Millimeter Array (IRAM NOEMA) program that mapped these lines.

5. CONCLUSION

In this paper, we study the molecular gas in starburst galaxy M82. We determine the varying physical conditions of M82's molecular gas, trace varying line ratios to uncover changes in gas conditions, and consider how our derived conditions depend on the model prescription. To summarize, we find that line ratios vary significantly on both a high resolution and low resolution scale, specifically closer to the center. The varying line ratios reveal hidden changes in molecular gas conditions in M82, including changes in excitation conditions, abundance, and optical depth. To identify the physical conditions of the gas and explore the implications of utilizing sophisticated models, we present a one zone model, log-normal density distribution model and a novel log-normal temperature distribution model. Using non-LTE simulations, we create a grid of simulated intensities that were compared to observed ratios. We consider the effect that such sophisticated models have on our inferred physical parameters. We see that log-normal models predict similar results that align with line ratio analysis and that one zone modeling generally predicts lower temperatures (on average, by 44%) and higher densities (on average, by 50%). We also find that derived $\log N_{\text{CO}}$ values from all three models agree. We identify the following conditions of the gas in the central molecular zone of M82: $T_{\text{kin}} \sim 65\text{K}$, $\log(n_{\text{H}_2}[\text{cm}^{-3}]) \sim 3.5$, and $\log(N_{\text{CO}}[\text{cm}^{-2}]) \sim 18.1$. We reveal possible degeneracies in distribution widths and between density and temperature. Finally, we study the relationship between observations and the one zone modeling fit under the assumption that the molecular gas is in LTE. We conclude that the implementation of sophisticated models results in significantly different derived parameters, elucidating the importance of introducing models that incorporate varied temperatures.

Beyond the immediate relevance to advancing the study of molecular gas composition in starburst galaxies, our work also sheds light on galaxies at the peak of cosmic star formation. At redshift $z = 2$, the average SFR in the Universe was 10 times higher than today (Madau & Dickinson 2014). The mechanism behind this high star formation is an open question in astronomy: was the higher SFR driven by higher star forming efficiency, or driven by a larger reservoir of molecular gas? By analyzing current starburst galaxies, as we have done in this paper, we can probe the nature of such extreme galaxies from our past (Bian et al. 2016). Therefore, analyzing current starburst galaxies allows us to probe the extreme star forming nature of galaxies once in our universe. Exploring the relationship between our work and the history of cosmic star formation offers an exciting prospect for additional future work. Another open question pertains to the driving process behind galaxy evolution in general. Galaxy evolution is closely linked to the baryon life cycle. In this work, we address one key component of this cycle: how molecular gas transforms into stars. In recent decades, collaborations like Physics at High Angular resolution in Nearby Galaxies (PHANGS) have emphasized studying the different steps of the baryon life cycle in the nearby universe and started combing them using multi wavelength observations (Leroy et al. 2021). Finally, even more broadly speaking, since we study molecular gas at extremely cold temperatures ($< 50\text{ K}$) and low densities ($< 10^4\text{ cm}^{-3}$), our findings enable us to probe conditions in the universe that do not exist on Earth and are not reproducible in laboratories.

6. ACKNOWLEDGMENTS

I am incredibly grateful to my mentor Dr. Jakob den Brok for his support throughout this project. Without his guidance and insightful feedback, my project would not be where it is today. I am also incredibly grateful to Dr. Qizhou Zhang for his willing support and advice, as well as welcoming me into his research group. Lastly, thank you to the Center for Astrophysics | Harvard & Smithsonian for supporting this research internship.

Facilities: IRAM30M, JCMT, NRO45M, SMA

APPENDIX

A. MOMENT CALCULATIONS AND PLOTS

Moments are calculated as follows. Moment 0 is obtained by integrating (collapsing) along the velocity axis with a channel width of δv :

$$W(x, y) = \sum_i M(x, y, v_i) T_{\text{mb}}(x, y, v_i) \delta v \quad [\text{Kkms}^{-1}]. \quad (\text{A1})$$

Pixels outside the mask, $M(x, y, v)$, are set to 0. Moment 1 can be calculated by

$$\bar{v}(x, y) = \frac{1}{W(x, y)} \sum_i v_i T_{\text{mb}}(x, y, v_i) M(x, y, v_i) \delta v \quad [\text{km s}^{-1}]. \quad (\text{A2})$$

Moment 2 can be calculated by

$$\sigma_v(x, y) = \left(\frac{1}{W(x, y)} \sum_i (v_i - \bar{v})^2 T_{\text{mb}}(x, y, v_i) M(x, y, v_i) \delta v \right)^{1/2}. \quad (\text{A3})$$

Figures 18, 19, and 20 show the moment 0, moment 1, and moment 2, respectively, of all observed low resolution lines. Again, the x and y axis for all three figures is the difference in right ascension and declination as measured from the center of the galaxy determined by Jackson et al. (2007).

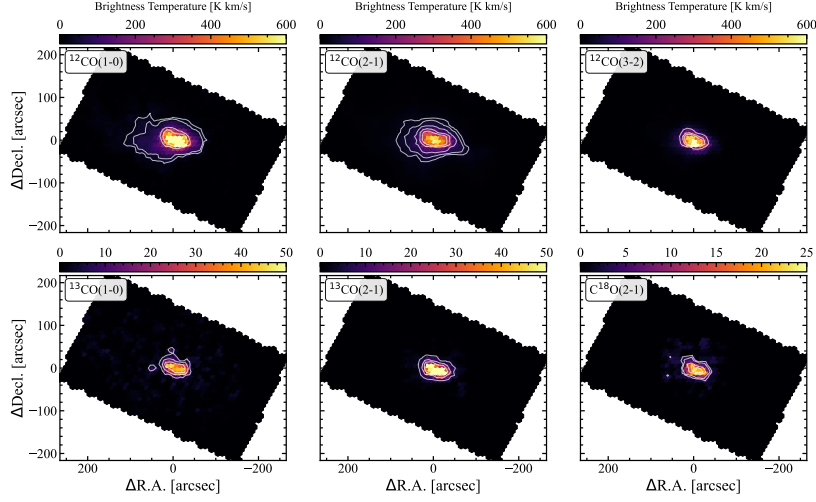


Figure 18. Moment 0 For Low Resolution Data. In other sections, we refer to Moment 0 as Brightness Temperature.

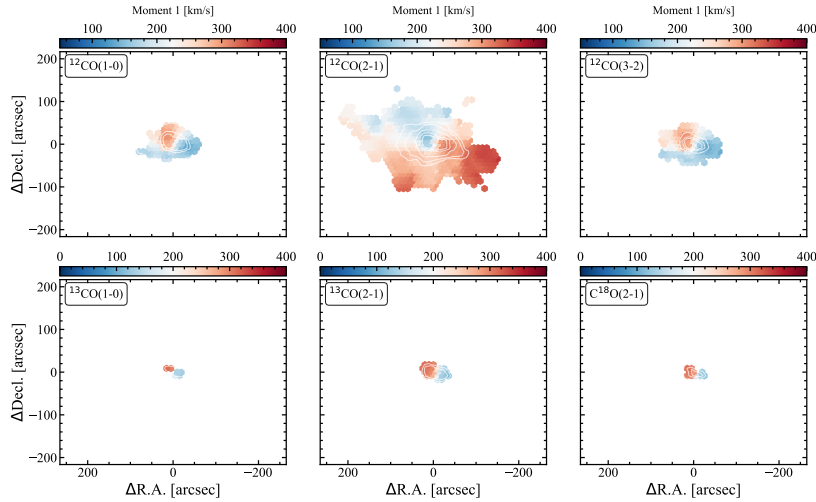


Figure 19. Moment 1 For Low Resolution Data.

B. MULTI-LINE MODELING VISUALIZATION – EDUCATIONAL TOOL

To contextualize the effect of individual free parameters (temperature, CO column density, H₂ volume density, and distribution width), we create an interactive educational visualization tool² in Bokeh, a Python library. We created

² Tool can be found at <http://localhost:5006/densityslider> and <http://localhost:5006/tempslider>

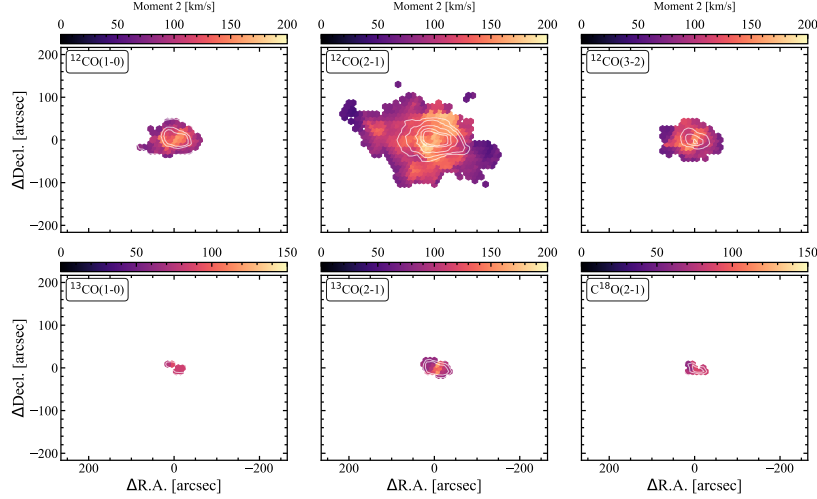


Figure 20. Moment 2 For Low Resolution Data. The pixels analyzed in 3.3.2 were those in which moment 2 of $^{13}\text{CO}(2-1)$ was defined.

two interactive web-plugins, one for each of the log-normal models. Such a visualization offers great educational value in understanding the link between the modeled free parameters and the simulated multi-line ratios. Specifically, the crux of the tool is to illustrate the impact of the various parameters and the implementation of a log-normal model on the simulated intensity ratios. The plugin allows users to toggle through different values of σ , T_{kin} , $\log N_{\text{CO}}$, and $\log n_{\text{H}_2}$ and explore their effects. Figures 21 and 22 show snapshots of the tools in action. In the top left corner, we can see toggles that can be slid through. The right panel shows the value of 8 pre-selected line ratios commonly observed in literature across nearby galaxies. The panels transform when the toggles move. While the tool holds educational value and power in visualization, the tool cannot replace the χ^2 analysis. One still needs to fit the simulated ratios to observations with Bayesian analysis (see 2.4) to determine which conditions best reproduce observations.

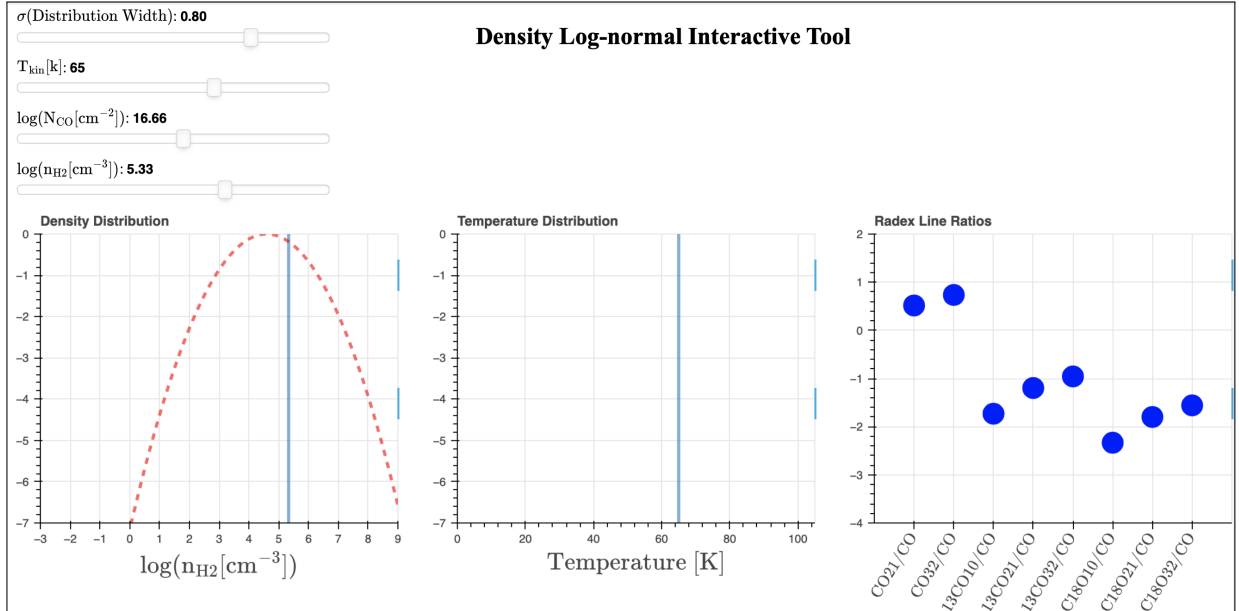


Figure 21. Bokeh Tool for Density Log-normal. The left and middle panel show the chosen distributions for T_{kin} and $\log n_{\text{H}_2}$. The right panel shows, in log scale, the values of 8 line ratios when we implement a density log-normal and have initial conditions of $\sigma = 0.8$, $T_{\text{kin}} = 65$, $\log N_{\text{CO}} = 16.66$, and $\log n_{\text{H}_2} = 5.33$.

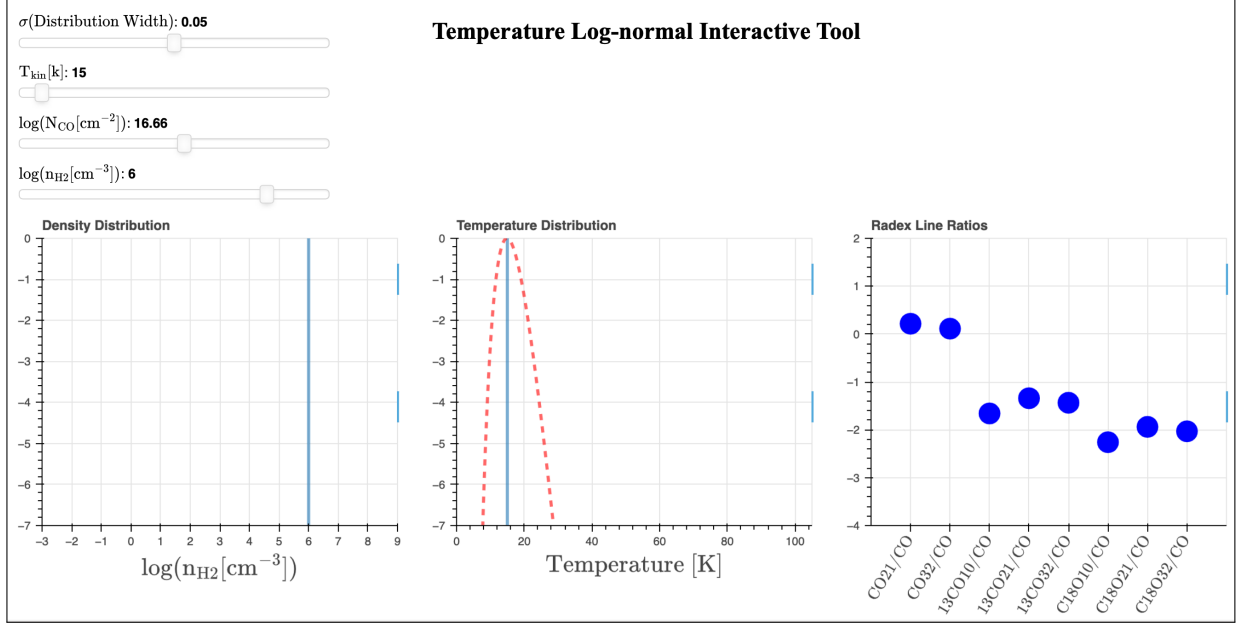


Figure 22. Bokeh Tool for Temperature Log-normal. The left and middle panel show the chosen distributions. The right panel shows, in log scale, the values of 8 line ratios when we implement a temperature log-normal and have initial conditions of $\sigma = 0.05$, $T_{\text{kin}} = 15$, $\log N_{\text{CO}} = 16.66$, and $\log n_{\text{H}_2} = 6$.

C. LTE CALCULATIONS

We use the following equations from [Nishimura et al. \(2015\)](#) in 3.4 to calculate excitation temperatures. The equation below calculates the $J = 2 - 1$ excitation temperature.

$$T_{\text{ex}}^{2-1} = 11.06 \left\{ \ln \left[1 + \frac{11.06}{T_{\text{peak}}^{12,2-1} + 0.19} \right] \right\}^{-1} \quad (\text{C4})$$

The equation below calculates optical depth.

$$\tau_{J=2}^{13}(\nu) = -\ln \left\{ 1 - \frac{T_{\text{mb}}^{13,2-1}(\nu)}{10.58} \left[\frac{1}{\exp(10.58/T_{\text{ex}}) - 1} - 0.02 \right]^{-1} \right\} \quad (\text{C5})$$

To calculate column densities under the assumption of LTE, we use equations from [Wilson et al. \(2014\)](#). We have

$$N(\text{total})_{\text{CO}}^{13} = 1.5 \times 10^{14} \frac{T \exp\{5.3/T\} \int \tau^{13}(\nu) d\nu}{1 - \exp\{-10.6/T\}}. \quad (\text{C6})$$

We assume that in the limit of optically thin lines, integrals that involve $\tau(\nu)$ are equal to the integrated line intensity $\int_{-\infty}^{\infty} T_{\text{MB}}(\nu) d\nu$, which is then further equal to our calculated moment 0. Then, we have

$$T \int_{-\infty}^{\infty} \tau(\nu) d\nu \cong \frac{\tau_0}{1 - e^{-\tau_0}} W(x, y), \quad (\text{C7})$$

where τ_0 is the peak optical depth calculated from Equation C5 and $W(x, y)$ is the moment 0. Then, our final ^{13}CO column density is

$$N(\text{total})_{\text{CO}}^{13} = 1.5 \times 10^{14} \frac{\exp\{5.3/T\}}{1 - \exp\{-10.6/T\}} \frac{\tau_0}{1 - e^{-\tau_0}} W(x, y). \quad (\text{C8})$$

We then convert from ^{13}CO column density to ^{12}CO density by multiplying $N(\text{total})_{\text{CO}}^{13}$ by abundance ratio $X_{12/13}$ of 50.

REFERENCES

- Areal, M. B., Paron, S., Celis Peña, M., & Ortega, M. E. 2018, *A&A*, 612, A117, doi: [10.1051/0004-6361/201732067](https://doi.org/10.1051/0004-6361/201732067)
- Bian, F., Kewley, L. J., Dopita, M. A., & Juneau, S. 2016, *ApJ*, 822, 62, doi: [10.3847/0004-637X/822/2/62](https://doi.org/10.3847/0004-637X/822/2/62)
- Blanton, M. R., Bershad, M. A., Abolfathi, B., et al. 2017, *AJ*, 154, 28, doi: [10.3847/1538-3881/aa7567](https://doi.org/10.3847/1538-3881/aa7567)
- Dabrowski, I. 1984, *Canadian Journal of Physics*, 62, 1639, doi: [10.1139/p84-210](https://doi.org/10.1139/p84-210)
- Davis, T. A. 2014, *MNRAS*, 445, 2378, doi: [10.1093/mnras/stu1850](https://doi.org/10.1093/mnras/stu1850)
- den Brok, J. S. 2022, PhD thesis, Bonn
- Eckart, A., Downes, D., Genzel, R., et al. 1990, *ApJ*, 348, 434, doi: [10.1086/168252](https://doi.org/10.1086/168252)
- Elia, D., Molinari, S., Schisano, E., et al. 2022, *ApJ*, 941, 162, doi: [10.3847/1538-4357/aca27d](https://doi.org/10.3847/1538-4357/aca27d)
- Elmegreen, B. G., & Scalo, J. 2004, *ARA&A*, 42, 211, doi: [10.1146/annurev.astro.41.011802.094859](https://doi.org/10.1146/annurev.astro.41.011802.094859)
- Förster Schreiber, N. M., Genzel, R., Lutz, D., & Sternberg, A. 2003, *ApJ*, 599, 193, doi: [10.1086/379097](https://doi.org/10.1086/379097)
- Israel, F. P. 2009, *A&A*, 506, 689, doi: [10.1051/0004-6361/200811586](https://doi.org/10.1051/0004-6361/200811586)
- . 2020, *A&A*, 635, A131, doi: [10.1051/0004-6361/201834198](https://doi.org/10.1051/0004-6361/201834198)
- Jackson, N., Battye, R. A., Browne, I. W. A., et al. 2007, *MNRAS*, 376, 371, doi: [10.1111/j.1365-2966.2007.11442.x](https://doi.org/10.1111/j.1365-2966.2007.11442.x)
- Kollmeier, J., Anderson, S. F., Blanc, G. A., et al. 2019, in *Bulletin of the American Astronomical Society*, Vol. 51, 274
- Krumholz, M. R., & McKee, C. F. 2005, *ApJ*, 630, 250, doi: [10.1086/431734](https://doi.org/10.1086/431734)
- Langer, W. D., & Penzias, A. A. 1990, *ApJ*, 357, 477, doi: [10.1086/168935](https://doi.org/10.1086/168935)
- Leroy, A., Schinnerer, E., Hughes, A., et al. 2021, in *American Astronomical Society Meeting Abstracts*, Vol. 53, American Astronomical Society Meeting Abstracts, 124.06
- Leroy, A. K., Usero, A., Schrubba, A., et al. 2017, *ApJ*, 835, 217, doi: [10.3847/1538-4357/835/2/217](https://doi.org/10.3847/1538-4357/835/2/217)
- Lianou, S., Barmby, P., Mosenkov, A. A., Lehnert, M., & Karczewski, O. 2019, *A&A*, 631, A38, doi: [10.1051/0004-6361/201834553](https://doi.org/10.1051/0004-6361/201834553)
- Madau, P., & Dickinson, M. 2014, *ARA&A*, 52, 415, doi: [10.1146/annurev-astro-081811-125615](https://doi.org/10.1146/annurev-astro-081811-125615)
- Mao, R. Q., Henkel, C., Schulz, A., et al. 2000, *A&A*, 358, 433, doi: [10.48550/arXiv.astro-ph/0005499](https://doi.org/10.48550/arXiv.astro-ph/0005499)
- Meier, D. S., Turner, J. L., & Beck, S. C. 2001, *AJ*, 122, 1770, doi: [10.1086/323136](https://doi.org/10.1086/323136)
- Michiyama, T., Iono, D., Sliwa, K., et al. 2018, *ApJ*, 868, 95, doi: [10.3847/1538-4357/aae82a](https://doi.org/10.3847/1538-4357/aae82a)
- Nishimura, A., Tokuda, K., Kimura, K., et al. 2015, *ApJS*, 216, 18, doi: [10.1088/0067-0049/216/1/18](https://doi.org/10.1088/0067-0049/216/1/18)
- Nishimura, Y., Watanabe, Y., Harada, N., Kohno, K., & Yamamoto, S. 2019, *ApJ*, 879, 65, doi: [10.3847/1538-4357/ab24d3](https://doi.org/10.3847/1538-4357/ab24d3)
- Padoan, P., & Nordlund, Å. 2002, *ApJ*, 576, 870, doi: [10.1086/341790](https://doi.org/10.1086/341790)
- Schöier, F. L., van der Tak, F. F. S., van Dishoeck, E. F., & Black, J. H. 2005, *A&A*, 432, 369, doi: [10.1051/0004-6361:20041729](https://doi.org/10.1051/0004-6361:20041729)
- Seaquist, E. R., & Frayer, D. T. 2000, *ApJ*, 540, 765, doi: [10.1086/309378](https://doi.org/10.1086/309378)
- Shetty, R., Glover, S. C., Dullemond, C. P., et al. 2011, *MNRAS*, 415, 3253, doi: [10.1111/j.1365-2966.2011.18937.x](https://doi.org/10.1111/j.1365-2966.2011.18937.x)
- Shimajiri, Y., Kitamura, Y., Saito, M., et al. 2014, *A&A*, 564, A68, doi: [10.1051/0004-6361/201322912](https://doi.org/10.1051/0004-6361/201322912)
- Shirley, Y. L. 2015, *PASP*, 127, 299, doi: [10.1086/680342](https://doi.org/10.1086/680342)
- Sofue, Y. 1998, *PASJ*, 50, 227, doi: [10.1093/pasj/50.2.227](https://doi.org/10.1093/pasj/50.2.227)
- Tan, Q.-H., Gao, Y., Zhang, Z.-Y., & Xia, X.-Y. 2011, *Research in Astronomy and Astrophysics*, 11, 787, doi: [10.1088/1674-4527/11/7/005](https://doi.org/10.1088/1674-4527/11/7/005)
- Teng, Y.-H., Sandstrom, K. M., Sun, J., et al. 2022, *ApJ*, 925, 72, doi: [10.3847/1538-4357/ac382f](https://doi.org/10.3847/1538-4357/ac382f)
- Togi, A., & Smith, J. D. T. 2016, *ApJ*, 830, 18, doi: [10.3847/0004-637X/830/1/18](https://doi.org/10.3847/0004-637X/830/1/18)
- van der Tak, F. F. S., Black, J. H., Schöier, F. L., Jansen, D. J., & van Dishoeck, E. F. 2007, *A&A*, 468, 627, doi: [10.1051/0004-6361:20066820](https://doi.org/10.1051/0004-6361:20066820)
- van Dishoeck, E. F., & Black, J. H. 1986, in *Interstellar Processes: Abstracts of Contributed Papers*, ed. D. J. Hollenbach & J. Thronson, H. A., 149–150
- Vazquez-Semadeni, E., Passot, T., & Pouquet, A. 1994, in *American Astronomical Society Meeting Abstracts*, Vol. 185, American Astronomical Society Meeting Abstracts, 97.03
- Ward, J. S., Zmuidzinas, J., Harris, A. I., & Isaak, K. G. 2003, *ApJ*, 587, 171, doi: [10.1086/368175](https://doi.org/10.1086/368175)
- Weiß, A., Neininger, N., Henkel, C., Stutzki, J., & Klein, U. 2001, *ApJL*, 554, L143, doi: [10.1086/321711](https://doi.org/10.1086/321711)
- Wilson, T., Rohlf, K., & Hüttemeister, S. 2014, *Tools of Radio Astronomy* (Springer)
- Wouterloot, J. G. A., Henkel, C., Brand, J., & Davis, G. R. 2008, *A&A*, 487, 237, doi: [10.1051/0004-6361:20078156](https://doi.org/10.1051/0004-6361:20078156)